The Astrophysical Journal, 926:55 (30pp), 2022 February 10 https://doi.org/10.3847/1538-4357/ac37b7
© 2022. The Author(s). Published by the American Astronomical Society.
OPEN ACCESS

SOFIA Observations of Far-IR Fine-structure Lines in Galaxies to Measure Metallicity

Luigi Spinoglio[1], Juan Antonio Fernández-Ontiveros[1,2], Matthew A. Malkan[3], Suyash Kumar[3], Miguel Pereira-Santaella[4], Borja Pérez-Díaz[5], Enrique Pérez-Montero[5], Alfred Krabbe[6], William Vacca[7], Sebastian Colditz[6], and Christian Fischer[6]

[1] Istituto di Astrofisica e Planetologia Spaziale—INAF, Via Fosso del cavaliere 100, I-00133, Roma, Italy; luigi.spinoglio@inaf.it
[2] Centro de Estudios de Física del Cosmos de Aragón, Unidad Asociada al CSIC, Plaza San Juan 1, E-44001 Teruel, Spain
[3] Department of Physics and Astronomy, UCLA, Los Angeles, CA 90095-1547, USA
[4] Centro de Astrobiología (CSIC-INTA), Ctra. de Ajalvir, Km 4, E-28850, Torrejón de Ardoz, Madrid, Spain
[5] Instituto de Astrofísica de Andalucía (IAA-CSIC), Glorieta de la Astronomía s/n, E-18008 Granada, Spain
[6] Deutsches SOFIA Institut, University of Stuttgart, Pfaffenwaldring 29, D-70569 Stuttgart, Germany
[7] SOFIA/USRA, NASA Ames Research Center, MS N232-12, Moffett Field, CA 94035-1000, USA
Received 2021 August 7; revised 2021 October 22; accepted 2021 November 7; published 2022 February 11

Abstract

We present new and archival SOFIA FIFI-LS far-IR spectroscopic observations of the [O III] 52 μm and/or the [N III] 57 μm lines of 25 local galaxies. Including 31 other galaxies from Herschel-PACS, we discuss a local sample of 47 galaxies, including the H II galaxies, luminous IR galaxies, low-metallicity dwarfs, and Seyfert nuclei. Analyzing the mid- to far-IR fine-structure lines of this sample, we assess the metallicity and compare it with the optical spectroscopy estimates. Using the IR, we find an O/H–N/O relation similar to that known in the optical. Conversely, we find systematically lower N/O IR abundances when compared to the optical determinations, especially at high values of N/O ($\log(N/O) > -0.8$). We explore various hypotheses to account for this difference: (i) difference in ionization structure traced by optical (O^+, N^+ regions) versus IR lines (O^{2+}, N^{2+} regions), (ii) contamination of diffuse ionized gas affecting the optical lines used to compute the N/O abundance, and (iii) dust obscuration affecting the optical-based determinations. However, we have not found any correlation of $\Delta(N/O) = (N/O)_{OPT} - (N/O)_{IR}$ with ionization, or electron density, or optical extinction. We speculatively suggest that the accretion of metal-poor gas from the circumgalactic medium could provide an explanation for this difference because the rapid decrease of total abundances during infall is followed by a N/O ratio decrease due to the primary production of young—possibly embedded—massive stars, which are preferentially traced by the IR diagnostics, while optical diagnostics would better trace the secondary production, when both N/O and O/H abundance ratios increase.

Unified Astronomy Thesaurus concepts: Galaxy abundances (574)

Supporting material: figure set

1. Introduction

The content of heavy elements in galaxies is a key physical diagnostic of galaxy evolution because metals are a by-product of star formation activity. Additionally, the metal abundances are modulated by inflow and outflow events, which involve both starburst and active galactic nucleus feeding and feedback processes. It has long been known that massive galaxies have higher metallicities compared to galaxies with lower stellar mass (Lequeux et al. 1979; Tremonti et al. 2004). More recently, the cosmic evolution of this correlation was measured out to high redshifts (Henry et al. 2013; Ly et al. 2016; see Maiolino & Mannucci 2019 and references therein for a review). Aside from the global metallicity, as measured by the O/H ratio, the relative abundances between heavy elements are also a key tool to understand the chemical evolution of galaxies (e.g., Pérez-Montero et al. 2013). One of the main problems that still need to be explored is the behavior of the N/O ratio, which is dominated by primary oxygen and nitrogen production in young stellar populations. When these evolve during the lifetime of the galaxy, the nitrogen abundance is increased by the secondary production due to the yield of intermediate-mass stars (Dopita & Evans 1986; Pilyugin et al. 2003; Vila-Costas & Edmunds 1993; Vincenzo et al. 2016). Furthermore, the N/O ratio depends on the star formation efficiency (e.g., Mollá et al. 2009), the accretion of pristine external gas (Amorín et al. 2010; Perez et al. 2011; Torrey et al. 2012), the efficiency of galactic winds in removing metals from the interstellar medium (ISM; e.g., Hogarth et al. 2020), and on the shape of the initial mass function (IMF) (e.g., Tsujimoto & Bekki 2011). Therefore, while O/H provides information on the total amount of heavy elements produced, the N/O ratio tells us how these elements have been formed.

The earliest galaxies are likely to have very strong high-ionization emission lines. At their high redshifts ($z > 4$), their key diagnostic, fine-structure forbidden lines, can be detected at submillimeter wavelengths by ALMA (De Breuck et al. 2019). To understand the abundances in the ionized ISM in these high-redshift galaxies, we need more and better observations of the same far-IR fine-structure lines in local galaxies and especially in nearby dwarf galaxies, characterized by low metal abundances.

Nearly all studies of the gas metallicity in galaxies have used rest-frame optical and UV diagnostics (e.g., Nagao et al. 2006; Kewley & Ellison 2008, and references therein). However, optical/UV spectroscopic methods to derive gas metallicity have several limitations: (i) optical/UV diagnostics cannot probe the metallicity of the regions affected by significant dust

Original content from this work may be used under the terms of the Creative Commons Attribution 4.0 licence. Any further distribution of this work must maintain attribution to the author(s) and the title of the work, journal citation and DOI.

extinction or of dust-obscured galaxies; (ii) the emissivity of optical and UV permitted or forbidden lines depends strongly on the gas temperature because the atomic levels involved in the transitions are highly excited above the ground level; (iii) nebular diagnostics using the optical [N II] lines can introduce biases, e.g., in the O/H abundances and the ionization parameter, for sources with high or low N/O abundances (Pérez-Montero & Contini 2009); (iv) when applied to nebular lines in active galactic nuclei (AGNs), the temperature method —widely used in star-forming regions—underestimates the metallicities by typically ∼0.8 dex when compared to estimates from strong-line methods (Dors et al. 2015). Additionally, a large fraction of oxygen in AGNs is expected to be highly ionized ($O^{>2+}$) and therefore not traced by optical transitions (Pérez-Montero et al. 2019). All of these limitations are overcome by using the IR fine-structure lines, as was shown using observations of planetary nebulae (Pottasch & Beintema 1999; Bernard-Salas et al. 2001; Liu et al. 2001) by the Short Wavelength Spectrometer (de Graauw et al. 1996) and the Long Wavelength Spectrometer (LWS; Clegg et al. 1996) on board the Infrared Space Observatory (ISO; Kessler et al. 1996).

The use of IR fine-structure line ratios for gas-metallicity diagnostics and in particular for measuring abundance ratios different from the solar values was pioneered by Spinoglio & Malkan (1992), who considered in their study H II region abundances and highly dust-depleted abundances using a standard photoionization code. More recently, metallicity diagnostics based on the far-IR fine-structure lines of [O III] 51.8μ m, [O III]88.3μ m, and [N III]57.2μm have been proposed as metallicity tracers by Nagao et al. (2011) and applied to Herschel-PACS observations of ultraluminous IR galaxies (ULIRGs) by Pereira-Santaella et al. (2017) and Herrera-Camus et al. (2018). The nebular ionization structure of oxygen and nitrogen species is expected to be nearly identical, due to the very similar ionization potential values of these elements (13.6 and 14.5 eV for O^+ and N^+, respectively, and 35.1 and 29.6 eV for O^{2+} and N^{2+}). This implies that the intensity ratios of O^{2+} and N^{2+} transitions can be used as a proxy for the global N/O abundance ratio. Nevertheless, this approach requires previous knowledge of the O/H–N/O relation to derive metallicities, which may present large deviations from the relation observed in the local universe, especially under extreme star formation conditions (e.g., Amorín et al. 2010).

Alternative IR-based tracers on the mid-IR lines of neon and sulfur were introduced by Fernández-Ontiveros et al. (2016, 2017) as potential tools to study the chemical evolution of galaxies at the cosmic noon through space-borne IR spectroscopy. However, a large improvement in the determination of IR abundances was achieved by exploiting the full suite of mid- to far-IR lines. This was recently implemented by Fernández-Ontiveros et al. (2021) to determine chemical abundances for star-forming galaxies by applying Bayesian techniques to a grid of photoionization models covering a wide range in O/H, N/O, and ionization parameter (U). Specifically, the N/O abundance can be fixed from the far-IR transitions of O^{2+} and N^{2+}, while the ionization-sensitive ratios of the neon and sulfur lines can be used to determine the metallicity using known empirical correlations between U and O/H (Pérez-Montero 2014) as priors.

In this work, we present the largest available sample of galaxies for which new far-IR spectroscopic observations of [O III] 52 μm and [N III] 57 μm lines have been collected with the Stratospheric Observatory for Infrared Astronomy (SOFIA), complemented by the work of Herschel-PACS. This unique spectroscopic catalog allows us to develop and test a new IR diagnostic for the global and relative abundances of heavy elements.

This paper is organized as follows. Section 2 presents the observations carried out with SOFIA (Temi et al. 2014), their data analysis procedure, and the ancillary data that we have assembled to complement and analyze the results. Section 3 used IR line-ratio diagrams to classify the galaxies of our sample according to the ionization and density of their line-emission regions using standard photoionization models. Section 4 outlines the two methods used to derive the abundances using optical lines and IR fine-structure lines. Section 5 gives the results of this work using various IR line-ratio diagrams to measure the metallicity, and a discussion is presented in Section 6. Finally, Section 7 gives the summary of this work.

2. Observations

We present new observations with the SOFIA Far Infrared Field-Imaging Line Spectrometer (FIFI-LS Fischer et al. 2018) for 25 galaxies. FIFI-LS is a mid-IR medium-resolution (R ∼ 500–2000) integral field spectrograph. It consists of two independently and simultaneously operated spectrographs and uses a dichroic to split incoming light into two channels: a blue side (50–125 μm) and a red side (100–205 μm). Each spectrograph contains an image slicer and a disperser that enables the simultaneous acquisition of spectra from 25 spatial positions. The detectors in both spectrographs consist of 400 (5 spatial × 5 spatial × 16 spectral) gallium-doped germanium pixels. The instantaneous spectral coverage of the 16 pixels ranges from 1000–3000 km s^{-1}. The blue-side spectrograph has an instantaneous field of view of 30″ × 30″ with 6″ spatial pixels (spaxels), while the red side has a field of view of 60″ × 60″ with 12″ spaxels. The field of view of the blue side is completely contained within that of the red side. A description of the properties of FIFI-LS can be found in Fischer et al. (2018), Colditz et al. (2020), and the SOFIA website.[8]

Among the SOFIA FIFI-LS observations presented here, the only published data are those for Arp 299, Haro 3, II Zw 40, M83, MCG+12-02-001, NGC 4194, and NGC 4214 and reported in Peng et al. (2021); however, we also performed a new analysis of these data in order to have a homogeneous data set. In most cases, we have found the results to be consistent (within the errors) with the values published by these authors, as can be seen in Tables 2 and 4. The only exceptions are for MCG+12-02-001, for which we adopted the [O III] 52 μm and [N III] 57 μm line fluxes published in Peng et al. (2021) because their results show a higher signal-to-noise ratio, and for II Zw 40, for which we find a significantly lower (by a factor ∼2) [O III] 52 μm line flux because of the more compact emission region that we have chosen (∼15″ in diameter) in this very compact galaxy compared to the more extended area sampled by Peng et al. (2021; ≳20″ in diameter). In this latter

[8] https://www.sofia.usra.edu/science/proposing-and-observing/observers-handbook-cycle-7/3-fifi-ls

Table 1
Journal of the SOFIA FIFI-LS Observations

Target (1)	R.A. (2)	Decl. (3)	z (4)	Type (5)	AOR ID (6)	Mission-ID (7)	PI (8)	Line (9)	T_{exp} (s) (10)
MCG+12-02-001	$00^h54^m03\overset{s}{.}6$	$+73^d05^m12^s$	0.015698	ULIRG	07_0209_11	2019-05-01_FI_F562	G. Stacey	[O III]$_{52\mu m}$	1320.96
MCG+12-02-001	" "	" "	"	"	07_0209_12	2019-05-01_FI_F562	G. Stacey	[N III]$_{57\mu m}$	1351.68
NGC 1365	$03^h33^m36\overset{s}{.}4$	$-36^d08^m26^s$	0.005457	S1.8	05_0111_3	2017-07-28_FI_F424	G. Stacey	[O III]$_{52\mu m}$	1843.20
IC 342	$03^h46^m48\overset{s}{.}5$	$+68^d05^m47^s$	0.000103	H II	03_0135_9	2015-03-26_FI_F205	K. Croxall	[O III]$_{52\mu m}$	967.68
NGC 1569	$04^h30^m49\overset{s}{.}0$	$+64^d50^m53^s$	−0.000347	Dwarf	87_0005_7	2014-04-22_FI_FO162	R. Klein	[O III]$_{52\mu m}$	14976.50
NGC 1569	" "	" "	"	"	07_0048_2	2019-05-02_FI_F563	J. Spilker	[N III]$_{57\mu m}$	2805.76
NGC 1614	$04^h34^m00\overset{s}{.}0$	$-08^d34^m45^s$	0.015938	H II	07_0209_14	2019-10-30_FI_F631	G. Stacey	[O III]$_{52\mu m}$	522.24
NGC 1614	" "	" "	"	"	07_0209_15	2019-10-30_FI_F631	G. Stacey	[N III]$_{57\mu m}$	1136.64
NGC 1808	$05^h07^m42\overset{s}{.}3$	$-37^d30^m46^s$	0.003319	H II	05_0111_3	2017-07-28_FI_F424	G. Stacey	[O III]$_{52\mu m}$	1751.04
II Zw 40	$05^h55^m42\overset{s}{.}7$	$+03^d23^m32^s$	0.002632	Dwarf	06_0225_5	2018-11-06_FI_F524	G. Stacey	[O III]$_{52\mu m}$	768.00
II Zw 40	" "	" "	"	"	06_0225_10	2018-11-06_FI_F524	G. Stacey	[N III]$_{57\mu m}$	1536.00
NGC 2146	$06^h18^m37\overset{s}{.}8$	$+78^d21^m25^s$	0.002979	H II	03_0135_2	2015-03-12_FI_F199	K. Croxall	[O III]$_{52\mu m}$	368.69
NGC 2146	" "	" "	"	"	03_0135_17	2015-03-12_FI_F199	K. Croxall	[N III]$_{57\mu m}$	307.228
NGC 2366	$07^h28^m55\overset{s}{.}5$	$+69^d13^m05^s$	0.000267	Dwarf	07_0239_6	2019-05-14_FI_F570	M.A. Malkan	[O III]$_{52\mu m}$	614.40
NGC 2366	" "	" "	"	"	07_0239_7	2019-05-14_FI_F570	M.A. Malkan	[N III]$_{57\mu m}$	614.40
He 2–10	$08^h36^m15\overset{s}{.}2$	$-26^d24^m34^s$	0.002912	Dwarf	70_0508_6	2017-02-25_FI_F378	A. Krabbe	[O III]$_{52\mu m}$	1658.88
UGC 5189	$09^h42^m54\overset{s}{.}7$	$+09^d29^m01^s$	0.01072	H II	07_0182_1	2019-05-09_FI_F568	T. Jones	[O III]$_{52\mu m}$	2211.84
M82	$09^h55^m52\overset{s}{.}2$	$+69^d40^m48^s$	0.000677	H II	70_0408_1	2016-02-25_FI_F280	A. Krabbe	[O III]$_{52\mu m}$	2918.40
M82	" "	""	"	"	70_0608_10	2018-11-08_FI_F526	A. Krabbe	[N III]$_{57\mu m}$	4177.92
Haro 3	$10^h45^m22\overset{s}{.}4$	$+55^d57^m38^s$	0.003149	Dwarf	06_0225_6	2018-11-07_FI_F525	G. Stacey	[O III]$_{52\mu m}$	1413.12
Mrk 1271	$10^h56^m09\overset{s}{.}1$	$+06^d10^m22^s$	0.00338	H II	07_0182_3	2019-05-04_FI_F565	T. Jones	[O III]$_{52\mu m}$	1720.32
Arp 299A	$11^h28^m30\overset{s}{.}4$	$+58^d34^m10^s$	0.0103	H II	05_0111_5	2017-02-28_FI_F379	G. Stacey	[O III]$_{52\mu m}$	2949.12
Arp 299B&C	" "	" "	"	"	05_0111_5	2017-02-28_FI_F379	G. Stacey	[O III]$_{52\mu m}$	2949.12
Pox 4	$11^h51^m11\overset{s}{.}6$	$-20^d36^m02^s$	0.01197	H II	07_0182_2	2019-05-03_FI_F564	T. Jones	[O III]$_{52\mu m}$	1259.52
Mrk 193	$11^h55^m28\overset{s}{.}3$	$+57^d39^m52^s$	0.017202	H II	07_0182_4	2019-05-14_FI_F570	T. Jones	[O III]$_{52\mu m}$	3164.16
NGC 4194	$12^h14^m09\overset{s}{.}5$	$+54^d31^m37^s$	0.008342	H II	07_0209_16	2019-05-09_FI_F568	G. Stacey	[O III]$_{52\mu m}$	430.08
NGC 4194	" "	" "	"	"	07_0209_18	2019-05-09_FI_F568	G. Stacey	[N III]$_{57\mu m}$	860.16
NGC 4214	$12^h15^m39\overset{s}{.}3$	$+36^d19^m37^s$	0.00097	Dwarf	06_0225_8	2019-02-28_FI_F549	G. Stacey	[O III]$_{52\mu m}$	1320.96
NGC 4214	" "	" "	"	"	06_0225_9	2019-05-08_FI_F567	G. Stacey	[N III]$_{57\mu m}$	1413.12
NGC 4536	$12^h34^m27\overset{s}{.}1$	$+02^d11^m17^s$	0.006031	H II	03_0135_6	2015-03-27_FI_F206	K. Croxall	[O III]$_{52\mu m}$	399.36
NGC 4631	$12^h42^m07\overset{s}{.}8$	$+32^d32^m35^s$	0.002021	H II	07_0239_3	2019-05-10_FI_F569	M.A. Malkan	[O III]$_{52\mu m}$	215.04
NGC 4631	" "	" "	"	"	07_0239_3	2019-05-10_FI_F569	M.A. Malkan	[N III]$_{57\mu m}$	1720.32
NGC 4670	$12^h45^m17\overset{s}{.}1$	$+27^d07^m31^s$	0.003566	Dwarf	06_0222_21	2019-03-02_FI_F551	T. Wiklind	[O III]$_{52\mu m}$	491.52
M83	$13^h37^m00\overset{s}{.}9$	$-29^d51^m56^s$	0.001711	H II	07_0209_8	2019-05-04_FI_F565	G. Stacey	[O III]$_{52\mu m}$	2119.68
NGC 5253	$13^h39^m56\overset{s}{.}0$	$-31^d38^m24^s$	0.001358	Dwarf	07_0239_4	2019-05-10_FI_F569	M.A. Malkan	[O III]$_{52\mu m}$	307.20
NGC 5253	" "	" "	"	"	07_0239_5	2019-05-10_FI_F569	M.A. Malkan	[N III]$_{57\mu m}$	829.44

case, we report our flux measurement for the [O III] 52 μm line, and we give an upper limit for the [N III]57 μm line.

For NGC 2146, we adopted the line flux from Brauher et al. (2008), who used the ISO-LWS spectrometer.

The journal of the SOFIA FIFI-LS observations that we have reduced is presented in Table 1, which gives detailed information on the SOFIA programs, including the astronomical observation request (AOR) identification, the Mission-ID, the PI of the program, the observed spectral line, and the total integration time. In total, we have analyzed the spectra of 25 galaxies. For eight of these galaxies, we have SOFIA detections of both the [O III] 52 μm and [N III] 57 μm lines, for another eight galaxies, we have combined the new [O III] 52 μm line detection from SOFIA with the [N III] 57 μm line observation from Herschel-PACS (see Table 2), while for the remaining nine galaxies we present detections of the [O III] 52 μm line only, which are not complemented by any observation of the [N III] 57 μm line (Table 4). The data have been reduced with the FIFI-LS pipeline (Vacca et al. 2020), and the reduced data cubes have been retrieved from the SOFIA archive at IRSA.[9]

[9] https://irsa.ipac.caltech.edu/Missions/sofia.html

2.1. Data Analysis

We present below our procedure for extracting emission-line fluxes and their uncertainties for the SOFIA FIFI-LS data. We could not use the standard paxel-by-paxel fitting procedure, used normally for integral field unit (IFU) data, because the high background contribution from the atmosphere drastically reduces the signal-to-noise ratio of our data sets.

We use here the example of NGC 5253, a galaxy observed within our program (PI M.A. Malkan; AOR ID 07_0239_4). All other galaxy spectra have been reduced using the same method. The data cubes used for these reductions have all been obtained from the SOFIA data archive, unless otherwise indicated.

To illustrate the position of the FIFI-LS observations, we obtained a 2MASS *H*-band All-Sky Release Survey Atlas Image of each galaxy over approximately the same spatial scale as that covered by FIFI-LS on SOFIA. In the special cases of NGC 2366 and UGC 5189, we present WISE *W1*-band images of these galaxies instead of the 2MASS images due to the lack of significant emission in the latter; refer to Figures 23.15 and 23.16. This is shown in Figure 1(a). The exact areas covered by FIFI are shown by the solid yellow and dotted salmon boxes

Table 2
Observed Far-IR Line Fluxes of the Local Galaxy Sample

Name	$F_{[O\ III]52\mu m}$ (10^{-17} W m^{-2})	$F_{[N\ III]57\mu m}$ (10^{-17} W m^{-2})	$F_{[O\ III]88\mu m}$ (10^{-17} W m^{-2})	$F_{[N\ II]122\mu m}$ (10^{-17} W m^{-2})	$F_{[N\ II]205\mu m}$ (10^{-17} W m^{-2})	Notes	References
(1)	(2)	(3)	(4)	(5)	(6)	(7)	(8)
Haro11	⋯	28.30 ± 0.80	172.0 ± 3.0	3.51 ± 0.27	2.34 ± 0.49	⋆	C15
NGC 253	⋯	599.5 ± 178.3	625.2 ± 53.5	802.7 ± 28.1	175.3 ± 11.2	⋆	FO16
MCG+12-02-001	305.0 ± 30.9	52.9 ± 15.3	234.0 ± 24.0	23.20 ± 1.12	⋯	‡	P21, B08, AH10
NGC 1068	369.4 ± 34.7	443.6 ± 41.9	634.3 ± 19.7	294.5 ± 3.0	186.6 ± 6.8	⋆	FO16
NGC 1365	72.43 ± 23.57	131.6 ± 16.7	200.3 ± 8.1	254.8 ± 3.8	77.97 ± 1.46	† #	FO16
NGC 1569	1237. ± 245.	152.2 ± 37.4	2800. ± 10.	⋯	⋯	‡ #	C15
NGC 1614	219.7 ± 71.1	46.8 ± 6.6	193.0 ± 12.1	⋯	10.62 ± 0.39	‡ #	FO16
NGC 1808	125.3 ± 39.9	152.6 ± 10.8	204.4 ± 11.0	271.2 ± 4.3	⋯	† #	FO16
II Zw 40	202.6 ± 46.7	58.2 ± 16.8	359.0 ± 4.0	<2.65	⋯	‡ #	P21, C15
Mrk 3	114.8 ± 46.5	19.6 ± 3.9	58.49 ± 2.94	10.20 ± 1.47	⋯	⋆	FO16
NGC 2146	1514. ± 201.	551. ± 59.	1577. ± 65.	459.3 ± 17.4	129.6 ± 1.9	⋆	B08, FO16
He 2–10	336.4 ± 54.6	98.5 ± 10.9	338.0 ± 5.0	⋯	10.42 ± 0.49	† #	C15
IRAS 08572+3915	⋯	2.4 ± 0.37	5.1 ± 0.26	0.74 ± 0.15	⋯	⋆	DS17
UGC 5101	⋯	10.13 ± 6.28	14.33 ± 3.36	13.16 ± 1.81	6.04 ± 0.44	⋆	FO16
M82	2915. ± 171.6	1620. ± 244.3	1991. ± 16.7	482.3 ± 5.4	437.6 ± 8.3	‡ #	FO16
NGC 3256	⋯	169.8 ± 13.8	461.1 ± 6.9	140.6 ± 2.0	45.27 ± 0.97	⋆	FO16
Haro 3	124.4 ± 17.8	12.3 ± 1.7	185.0 ± 4.0	2.14 ± 0.39	⋯	† #	C15
IRAS 10565+2448	⋯	9.10 ± 0.40	15.6 ± 0.40	8.1 ± 0.3	2.44 ± 0.13	⋆	PS17, P16
IRAS 11095-0238	4.80 ± 1.21	1.13 ± 0.77	⋯	1.05 ± 0.43	0.49 ± 0.16	⋆	FO16
Arp 299 A = IC 694	328.1 ± 37.0	73.0 ± 5.0	280.0 ± 3.2	10.05 ± 0.78	⋯	† #	C19
Arp 299 B+C = NGC 3690	246.8 ± 63.7	72.0 ± 1.3	300.0 ± 2.6	15.96 ± 0.38	⋯	† #	C19
NGC 4151	37.56 ± 9.56	21.73 ± 2.00	48.40 ± 2.87	7.09 ± 0.76	6.63 ± 0.68	⋆	FO16
IRAS 12112+0305	⋯	5.6 ± 0.9	7.4 ± 0.5	1.4 ± 0.4	⋯	⋆	PS17, DS17
NGC 4194	282.5 ± 14.6	65.0 ± 22.0	206.0 ± 14.0	<19.0	⋯	† #	B08
NGC 4214-reg.1	130.9 ± 11.7	19.30 ± 4.52	319.0 ± 6.2	4.4 ± 2.0	17.6 ± 0.53	‡ #	C19
NGC 4631	114.6 ± 30.7	160.1 ± 21.5	204.7 ± 4.3	36.74 ± 2.56	58.97 ± 1.47	‡ #	FO16
NGC 4945	<714	177. ± 16.	253. ± 60.	347.6 ± 9.7	⋯	⋆	FO16
NGC 5033	⋯	12.46 ± 2.10	25.79 ± 2.58	57.44 ± 1.71	⋯	⋆	FO16
IRAS 13120-5453	⋯	16.00 ± 3.84	30.08 ± 5.92	33.66 ± 3.00	10.62 ± 0.63	⋆	FO16, PS17
Cen A = NGC 5128	<462	53.34 ± 10.28	173.47 ± 6.68	85.15 ± 2.81	51.66 ± 1.47	⋆	FO16
M83	205.4 ± 18.7	166.5 ± 10.3	216.9 ± 6.97	321.0 ± 4.59	92.59 ± 3.90	† #	FO16
NGC 5253	412.0 ± 40.0	106.36 ± 20.6	901.0 ± 4.0	9.25 ± 1.21	⋯	‡#	C15
Mrk 273	⋯	13.78 ± 5.75	33.00 ± 5.53	8.58 ± 1.31	3.84 ± 0.28	⋆	FO16
IC 4329A	26.26 ± 2.59	9.31 ± 1.38	30.16 ± 1.31	3.31 ± 0.45	⋯	⋆	FO16
Mrk 463E	45.95 ± 7.92	9.61 ± 2.11	39.68 ± 4.13	2.31 ± 0.27	0.51 ± 0.20	⋆	FO16
Circinus	⋯	268.3 ± 15.3	565.5 ± 9.8	299.4 ± 4.0	⋯	⋆	FO16
NGC 5506	101.71 ± 20.12	30.79 ± 2.14	102.3 ± 3.3	14.14 ± 1.15	⋯	⋆	FO16
NGC 6240	46.57 ± 26.39	12.50 ± 5.86	33.10 ± 5.57	23.15 ± 2.22	18.47 ± 0.39	⋆	FO16
IRAS 17208-0014	⋯	10.72 ± 2.85	25.94 ± 4.61	9.84 ± 1.28	3.25 ± 0.24	⋆	FO16, PS17
3C 405 = Cyg A	78.58 ± 15.69	9.49 ± 3.8	28.04 ± 1.3	6.80 ± 0.46	1.68 ± 0.15	⋆	FO16
IRAS 20551-4250	⋯	4.0 ± 0.7	13.1 ± 0.4	2.3 ± 0.33	0.76 ± 0.11	⋆	PS17, DS17, P16
NGC 7130 = IC 5135	⋯	22.00 ± 5.49	19.58 ± 3.01	34.02 ± 1.86	13.94 ± 0.29	⋆	FO16
NGC 7172	⋯	6.96 ± 2.13	14.27 ± 2.49	11.74 ± 1.04	21.83 ± 0.58	⋆	FO16
NGC 7314	⋯	3.59 ± 0.44	15.19 ± 0.62	1.90 ± 0.19	⋯	⋆	FO16
NGC 7469	⋯	38.80 ± 9.88	37.03 ± 5.12	41.43 ± 1.48	11.45 ± 0.29	⋆	FO16
IRAS 23128-5919	⋯	17.1 ± 0.9	44.4 ± 0.7	4.4 ± 0.5	1.83 ± 0.10	⋆	P16, DS17
NGC 7582	139.8 ± 8.1	65.58 ± 10.23	201.9 ± 5.3	75.45 ± 2.04	19.59 ± 0.73	⋆	FO16

Notes. From left to right, the table columns show the (1) object name; (2), (3), (4), (5), (6) line fluxes, in units of 10^{-17} W m^{-2}, of the lines: $F_{[O\ III]52\mu m}$, $F_{[N\ III]57\mu m}$, $F_{[O\ III]88\mu m}$, $F_{[N\ II]122\mu m}$, and $F_{[N\ II]205\mu m}$; (7) origin of far-IR spectroscopy. All measurements of $F_{[N\ II]205\mu m}$ are from Herschel-SPIRE; ⋆: all data from Herschel-PACS; †: $F_{[O\ III]52\mu m}$ from SOFIA FIFI-LS; ‡: $F_{[O\ III]52\mu m}$ and $F_{[N\ III]57\mu m}$ from SOFIA FIFI-LS; #: SOFIA data reduced in this work. (11) Reference for the line fluxes: P21: Peng et al. (2021), C15: Cormier et al. (2015), C19: Cormier et al. (2019), B08: ISO-LWS data from Brauher et al. (2008); DS17: Díaz-Santos et al. (2017); FO16: Herschel-PACS data from Fernández-Ontiveros et al. (2016) and references therein; P16: Pearson et al. (2016), C. Pearson 2021, private communication; PS17: Pereira-Santaella et al. (2017).

(representing the regions covered for the [O III]52 μm and [N III]57 μm detections, respectively).

The first step to determine the line fluxes of each source is to define a useful aperture. We do have a spatial resolution of about FWHM $\sim$6″ and compact but still not point-like extension of the sources. We use the following procedure to find an ellipsoid-shaped aperture for each data set to capture the whole flux while minimizing the noise contribution of pixels without flux from the source.

We locate the emitting region of the galaxy in the far-IR using SOFIA line maps. The reduced data cube is a stack of 2D flux channel maps at various wavelengths. We integrate these maps across $\sim$10 wavelength channels surrounding the central redshifted wavelength of the emission line of interest. This

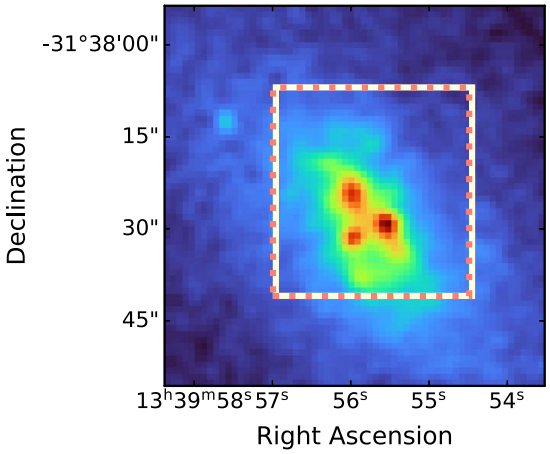

(a)

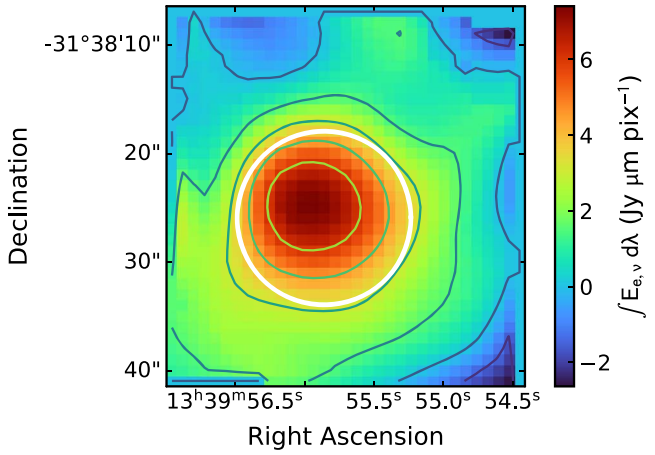

(b)

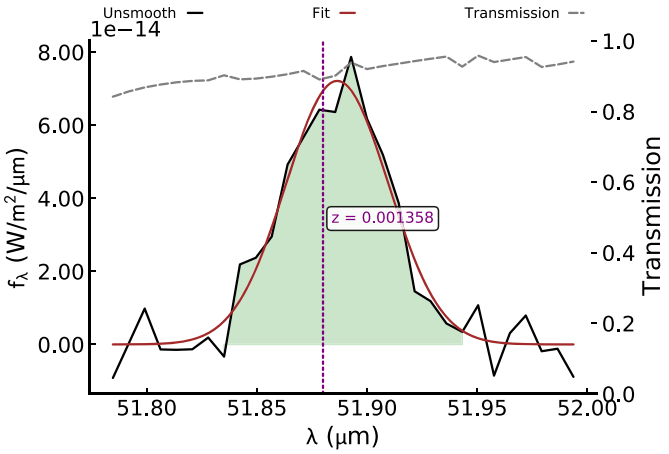

(c)

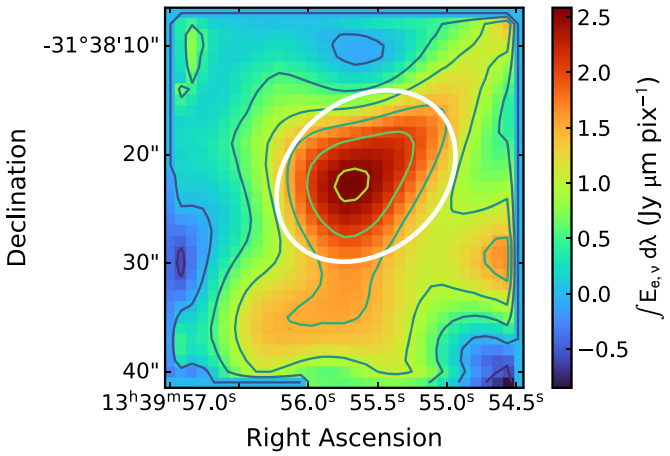

(d)

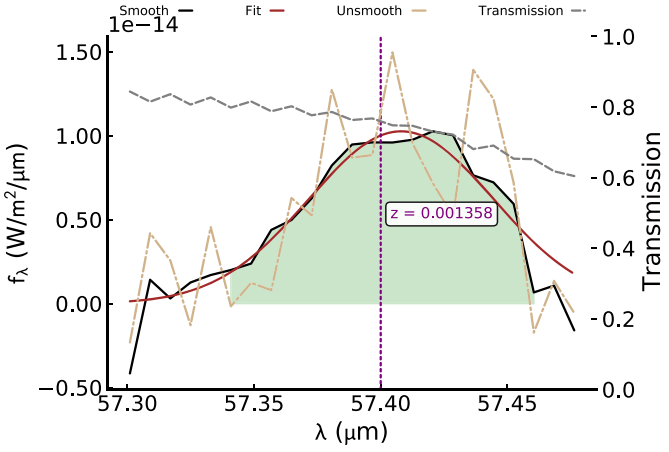

(e)

Figure 1. The 2MASS *H*-band image (Figure 1(a)), 2D line maps, and 1D spectra for [O III] 52 μm (Figures 1(b) and 1(c), respectively) and [N III] 57 μm (Figures 1(d) and 1(e), respectively) in NGC 5253. The [N III] 57 μm profiles here have not been corrected for atmospheric transmission.

gives us a preliminary line map for the galaxy that helps us locate its emitting region. After choosing a center (which often aligns closely with the optical center of the galaxy), we identify an elliptical aperture around the center that captures the majority of the emitting region. We add up the flux densities from all spaxels within this elliptical aperture and repeat this

procedure separately for all wavelengths to obtain the wavelength profile of the spectral density of the emission line.

Before calculating the emission-line flux, we trim our spectrum by masking out noisy wavelength channels on the red/blue side of the central wavelength. If the spectrum is still noisy, we apply a Wiener filter to it (this is the case with the [N III] 57 μm line, but not with the [O III]52 μm line in NGC 5253; see the solid black "smooth" line in Figure 1).

Thereafter, we typically identify 5–10 continuum points on either side of the central peak in the trimmed spectrum. We use the median of these values as the continuum signal and subtract it from all channels. We then add all channels that were considered to be part of the detection in the trimmed spectrum to create the continuum-subtracted line map (Figures 1(b) and 1(d)). After obtaining this line map, we may find that it sometimes differs from the preliminary continuum map we made for the galaxy. In such cases, we choose a new center and elliptical aperture that better matches the continuum-subtracted line map and repeat the above procedure. It is possible that in doing so, the choice of continuum points changes. But the difference is usually minor, and after a few iterations, we converge to a choice of center, elliptical aperture, and continuum points that together give the best possible continuum-subtracted line map with the chosen elliptical aperture best identifying the emitting region of the galaxy. Figures 1(b) and 1(d) were obtained through this iterative procedure.

We point out two caveats at this stage. First, while we generally use the flux channel from a data cube that has been corrected for atmospheric transmission (this is the case with the [O III] 52 μm line in NGC 5253), occasionally the atmospheric transmission in the wavelength range of interest can be low (notice the gray dashed line in Figure 1(e) with an atmospheric transmission as low as ~0.60). In these cases, we use the flux channel that has not been corrected for atmospheric transmission (this is the case with the [N III] 57 μm line in NGC 5253). We do so because the SOFIA archive's automated correction procedure does not handle low transmissions. Second, while circular apertures may suit compact objects that are nearly point like (e.g., the [O III] 52 μm line in NGC 5253), in other cases there is extended emission in certain directions, requiring an elliptical aperture to enclose most of the line-emitting region and maximize the signal-to-noise ratio. Standard software, like QFitsView,[10] supports only using circular apertures, so we wrote our own Python routine that can use elliptical apertures. The robustness of our routine has been verified by calculating fluxes independently for identical circular apertures created by QFitsView and our routine (using the procedure that will be described below) and checking that they are equal.

We now return to the trimmed spectrum that was obtained with the optimal choice of emission center, elliptical aperture, and continuum points to create the best continuum-subtracted line map for the galaxy. We then subtract off the continuum from the trimmed spectrum and fit a Gaussian to the resulting emission-line spectrum (solid brown lines in Figures 1(c) and 1(e)). This fitted Gaussian is overplotted with the solid black line in Figures 1(c) and 1(e). For Figure 1(e), where we applied the Wiener filter, we also include the unfiltered trimmed spectrum in the tan dotted–dashed line). Finally, we overplot the transmission line (gray dashed).

[10] https://www.mpe.mpg.de/~ott/QFitsView

We then measure the line flux, F, by integrating the area under the continuum-subtracted trimmed spectrum (green shaded area in Figures 1(c) and 1(e)). We exclude from this integration the spectral range used to estimate the continuum level. We then compute the formal statistical error δF in the flux as

$$\delta F = \Delta\lambda \sqrt{\sum_P (f(P) - y_P)^2}. \quad (1)$$

Here, P is a continuum point, y_P is its spectral density, and $f(P)$ is its spectral density as predicted by the fitted continuum line. $\Delta\lambda$ is the wavelength pixel width (which is 0.007 μm for SOFIA). Calculating δF amounts to adding the errors between the actual spectrum and the continuum line in quadrature. Note at this stage that if the flux channel used for the galaxy was not corrected for atmospheric transmission, we replace our calculated flux F with $F/\langle T\rangle$, where $\langle T\rangle$ is the average transmission in the wavelength range we integrate across to calculate F.

The formal statistical error does not take into account the uncertainty in setting the continuum level. To compute a more realistic error bar for our flux measurement, we make a slightly different choice of the continuum points in our trimmed spectrum (or alternatively make a somewhat different selection for the noise to discard from the untrimmed spectrum). This subjective estimate gives us a different, but still "nearly correct" continuum level. We repeat the aforementioned process to compute the flux with the formal statistical error again.

This leaves us with two flux readings, $F_1 \pm \delta F_1$ and $F_2 \pm \delta F_2$, from the two iterations. We are now ready to estimate the actual flux measurement as $F \pm \Delta F$, where

$$F = \frac{F_1 + F_2}{2} \quad (2)$$

and

$$\Delta F = \max(F_1, F_2) - \min(F_1, F_2) + \delta F_1 + \delta F_2. \quad (3)$$

Essentially, we are deriving our flux as the average of both estimates and the error as the difference of the upper bound and lower bound as dictated by the formal statistical error. This completes our data reduction process.

2.2. Ancillary Data

We have used the literature data to complement the observations obtained with SOFIA FIFI-LS. In particular, we have taken the catalog of Herschel (Pilbratt et al. 2010), PACS (Poglitsch et al. 2010), and SPIRE (Griffin et al. 2010) observations of AGN and starburst galaxies of Fernández-Ontiveros et al. (2016) and the observations of the dwarf galaxies of Cormier et al. (2015). We also included the ISO-LWS observations reported from Brauher et al. (2008) of NGC 2146 and NGC 4194. Our sample of local galaxies contains 47 galaxies divided in 21 H II region/(U)LIRG galaxies, 19 Seyfert galaxies, including 1 LINER and 7 dwarf galaxies. The sample is presented in Table 5, with all of the relevant information, including coordinates, redshift, optical metallicities, and N/O ratio, as computed from optical emission-line observations (Pérez-Montero 2014), as well as the abundances and the N/O ratio computed from the IR lines (Fernández-Ontiveros et al. 2021). The full data set of far-IR spectroscopy of the sample of 48 galaxies is given in Table 2.

We have also compiled the observations of the mid-IR fine-structure lines, mainly collected from the Spitzer (Werner et al. 2004) Infrared Spectrograph (IRS; Houck et al. 2004), as shown in Table 3. We note that this table contains 51 galaxies because we have also included 3 objects for which we do not have full far-IR lines coverage: IC 342, NGC 2976, and NGC 4536.

Table 4 presents the SOFIA FIFI-LS observations of the [O III]52 μm line of an additional list of 11 galaxies, for which we do not have detections of the [N III]57 μm line, and therefore we are not able to discuss them further.

3. Sample Characterization

We present in Figure 2 the so-called "IR BPT" diagram (Baldwin & Phillips 1981; BPT) proposed for the first time by Fernández-Ontiveros et al. (2016). In contrast with the optical BPT, the diagram in Figure 2 can be regarded as a "softness diagram" because the axes ([O IV] 25.9 μm/[O III] 88μm and [Ne III] 15.5μm/[Ne II] 12.8μm) are independent of the chemical abundances and thus represent a more selective measure of the strength and shape of the radiation field in the ~20–80 eV range (see also Vilchez & Pagel 1988; Pérez-Montero & Vílchez 2009; Meléndez et al. 2011). Here the separation of the different types of galaxies is largely independent of the photoionization models used to define the boundaries, mostly due to the high ionization potential of O^{3+} (54.9 eV). This is beyond the double ionization edge of helium (54.4 eV), where the continuum emission of any stellar population drops sharply while the AGN power-law continuum remains unaffected. Consequently, AGNs are in the right part of the diagram, characterized by a higher value of the ionization of the gas responsible for the emission, the H II region galaxies and (U)LIRG are on the lower-left part of the diagram, while the dwarf galaxies are at the upper-left region, having a metallicity significantly lower than solar. An additional advantage of IR diagnostics is that they are insensitive to dust extinction and temperature effects, in contrast to optical tracers.

The IR BPT represents a very powerful tool to separate galaxies not only by the shape of their primary ionizing spectrum, i.e., star formation or AGN dominated, using the [O IV] 25.9 μm/[O III] 88 μm line ratio, but also by the different metallicities, through the [Ne III] 15.5 μm/[Ne II] 12.8 μm line ratio. We use this diagram to further classify the Seyfert galaxies into two separate classes: those within the grid of AGN photoionization models (models A in Section 4) are classified hereafter as "AGN-dominated" galaxies, while those outside these models are called "other Seyfert galaxies". These latter galaxies include NGC 4945, NGC 5033, Cen A (NGC 5128), NGC 6240, NGC 7130 (IC 5135), NGC 7469, and NGC 7582. We note that for these galaxies the IR lines excitation can originate from, or at least be contaminated by, H II regions in the host galaxy (Xia et al. 2018).

In Figure 3 we show an ionization–density diagram made using the line ratios of [O III] 52 μm/88 μm and [Ne III] 15.5 μm/[Ne II] 12.8 μm. Two grids of starburst photoionization models (models B in Section 4) are shown, one with solar metal abundances and the other with subsolar abundances. The diagram shows that the typical density is ~$1.0 < \log(n_e/\mathrm{cm}^{-3}) < 3.0$, while the ionization parameter is $\sim -4 < \log(U) < -2$ for H II region galaxies/ULIRGs. The effect of decreasing the metal abundances is to shift the model grid to the right side of the diagram because the line ratio tracing the ionization parameter is sensitive to the metal abundances. The [Ne III] 15.5 μm/[Ne II] 12.8 μm ratio increases by an average factor of $\gtrsim$5, from solar to $0.4 \times Z_\odot$ abundances. We notice in Figure 3 that the three galaxies in this diagram classified as "other Seyfert" galaxies are well within the area populated by the H II region/ULIRG galaxies, confirming that most of their ionized emission do not originate in the AGN narrow-line region (NLR), as indicated by the low value of the ionization potential ($\log U \sim -3.5$).

Figure 4 shows another ionization–density diagram, made purely with far-IR lines, the [O III] 52 μm/88 μm ratio versus the [N III] 57 μm/[N II] 122 μm ratio. Similarly to the previous diagram, this diagram also indicates that the gas density is $\sim 1.0 < \log(n_e/\mathrm{cm}^{-3}) < 3.0$, and the ionization parameter is $\sim -4 < \log(U) < -2$. The effect of decreasing the metal abundances is to increase the ratio of [N III] 57 μm/[N II] 122 μm by an average factor of $\gtrsim$2.5, from solar to $0.4 \times Z_\odot$ abundances.

4. Photoionization Models and Abundance Determinations

In this work we have used various photoionization models using the CLOUDY code (Ferland et al. 2017), also with the aim to demonstrate their overall consistency with each other, which does not depend on the particular choices of the parameter details. One set of models (hereafter models A) has been taken from Fernández-Ontiveros et al. (2016), which includes both AGN models and starburst galaxy models. For the AGN, a grid of constant-density models (with $\log(n_\mathrm{H})$ $(\mathrm{cm}^{-3}) = 1$–6) in a plane-parallel geometry has been built using an AGN-ionizing continuum of a power law from the optical to the X-rays with a slope of $\alpha = -1.4$ ($S_\nu \propto \nu^\alpha$) and ionization parameters (U) with values of $\log U = -1.5, -2.0, -2.5, -3.0$, and -3.5. For these models, the maximum column density of $N_\mathrm{H} = 10^{23}$ cm^{-2} was used as the stopping criterion of the spatial integration, representative of the column density found in NLR clouds (Moore & Cohen 1994). For the star-forming galaxy models, the ionizing spectrum was simulated using the STARBURST99 code (Leitherer et al. 1999) for two cases: (1) a young burst of star formation with an age of 1 Myr and a metallicity of $Z = 0.004(1/5Z_\odot)$, in order to produce the hard UV-ionizing spectrum in a low-metallicity environment, such as the one typical of dwarf galaxies, and (2) a continuous burst of star formation with an age of 20 Myr and solar metallicity, to model normal star-forming galaxies. We use models with a plane-parallel geometry, constant pressure, initial densities in the $\log(n_\mathrm{H})$ $(\mathrm{cm}^{-3}) = 1$–6 range, and ionization parameters in the $\log U = -2.0$ to -4.5 range. We assumed two intervals for the Kroupa IMF (with exponents of 1.3 and 2.3 and mass boundaries of 0.1, 0.5, and 100 $M_\odot$), the 1994 Geneva tracks with standard mass-loss rates, and the Pauldrach/Hillier atmospheres, which take into account the effects of non-LTE and radiation-driven winds.

Another set of models (hereafter model B) has been taken from Pereira-Santaella et al. (2017) and includes both starburst galaxy and AGN models. In starburst models, they assumed a constant-pressure slab model illuminated by the spectrum of a continuous burst of star formation. This illuminating spectrum was calculated using STARBURST99 (Leitherer et al. 1999) assuming continuous star formation with a Kroupa (2001) IMF with an upper stellar-mass boundary of 100 $M_\odot$. This is an average spectrum representing the integrated emission of a

Table 3
Observed Mid-IR Fluxes of the Local Galaxy Sample

Name	Type	$F_{[S\ IV]10.5\mu m}$ (10^{-17} W m^{-2})	$F_{[Ne\ II]12.8\mu m}$ (10^{-17} W m^{-2})	$F_{[Ne\ III]15.5\mu m}$ (10^{-17} W m^{-2})	$F_{[S\ III]18.7\mu m}$ (10^{-17} W m^{-2})	$F_{[O\ IV]25.9\mu m}$ (10^{-17} W m^{-2})	$F_{[S\ III]33.5\mu m}$ (10^{-17} W m^{-2})	$F_{[Si\ II]34.8\mu m}$ (10^{-17} W m^{-2})	Refs.
(1)	(2)	(3)	(4)	(5)	(6)	(7)	(8)	(9)	(10)
Haro 11	Dwarf	49.4 ± 1.1	32.7 ± 0.9	112. ± 5.	53.1 ± 2.9	4.390 ± 0.784	81.7 ± 7.0	55.8 ± 4.5	C15
NGC 253	H II	<10.50	2832.30 ± 64.20	204.60 ± 9.60	666.40 ± 14.90	154.70 ± 26.90	1538.00 ± 30.10	2412.00 ± 48.00	FO16
MCG+12-02-001	LIRG	3.14 ± 0.81	201.10 ± 2.12	36.99 ± 0.67	73.46 ± 1.55	<6.36	167.60 ± 5.15	181.70 ± 9.64	I13
NGC 1068	S1h	536.10 ± 12.80	458.10 ± 13.80	1371.00 ± 10.20	240.60 ± 14.00	2030.00 ± 27.30	374.10 ± 23.20	604.40 ± 17.10	FO16
NGC 1365	S1	18.60 ± 0.78	143.00 ± 3.79	61.30 ± 0.51	51.20 ± 0.57	365.00 ± 26.90	720.00 ± 102.00	1303.00 ± 81.00	FO16
IC 342	H II	4.76 ± 0.66	615.46 ± 10.52	37.20 ± 0.90	320.03 ± 5.96	<7.70	672.46 ± 7.28	985.73 ± 10.29	FO16
NGC 1569	Dwarf	247. ± 3.	30.5 ± 2.7	324. ± 13.	131. ± 5.	31.9 ± 1.5	185. ± 6.	22.95 ± 1.19	C15
NGC 1614	H II	6.89 ± 0.54	249.00 ± 7.00	63.32 ± 1.59	83.03 ± 2.64	8.68 ± 0.85	101.06 ± 2.11	148.60 ± 4.11	FO16
NGC 1808	H II	1.47 ± 0.00	177.36 ± 16.36	17.26 ± 0.68	46.20 ± 2.29	<9.54	205.83 ± 20.27	354.26 ± 15.15	FO16
II Zw 40	Dwarf	200. ± 10.	7.35 ± 0.79	141. ± 9.	52.1 ± 2.2	7.94 ± 1.15	78.2 ± 2.1	36.8 ± 3.5	C15
Mrk 3	S1h	59.30 ± 0.62	98.00 ± 1.02	175.00 ± 1.10	53.60 ± 4.49	196.00 ± 2.40	52.40 ± 6.89	84.60 ± 3.28	FO16
NGC 2146	LIRG	6.30 ± 0.44	625.00 ± 15.35	91.16 ± 0.95	190.12 ± 4.15	19.33 ± 4.48	848.02 ± 36.93	1209.35 ± 21.70	FO16
He 2–10	Dwarf	32.7 ± 1.3	380.0 ± 13.0	156.0 ± 5.0	267.0 ± 19.0	7.915 ± 2.514	317.0 ± 10.0	193.0 ± 4.0	C15
IRAS 08572+3915	ULIRG	<0.5	8.36 ± 0.69	2.46 ± 0.50	1.84 ± 0.51	<2.1	<7.7	⋯	A07,V09
UGC 5101	ULIRG	1.32 ± 0.32	37.43 ± 0.45	14.05 ± 0.18	8.46 ± 0.20	7.34 ± 0.83	13.91 ± 1.39	27.47 ± 3.31	I13
NGC 2976	H II	⋯	6.3 ± 0.6	2.2 ± 0.2	5.1 ± 0.3	0.3 ± 0.1	7.5 ± 0.2	6.9 ± 0.4	D06
M82	H II	5.65 ± 0.74	506.22 ± 45.04	80.98 ± 1.99	172.06 ± 5.80	45.67 ± 6.61	1812.90 ± 36.79	2166.00 ± 25.52	FO16
NGC 3256	H II	5.25 ± 0.57	514.19 ± 9.34	64.42 ± 0.86	171.83 ± 2.07	12.23 ± 3.02	484.64 ± 13.79	623.37 ± 9.81	?
Haro 3	Dwarf	40.8 ± 1.7	35.2 ± 1.3	98.4 ± 7.4	50.3 ± 3.9	1.79 ± 0.5	85.1 ± 2.4	39.9 ± 2.4	C15
IRAS 10565+2448	ULIRG	<1.25	61.75 ± 0.81	7.67 ± 0.42	12.35 ± 1.01	<2.40	19.31 ± 1.53	39.88 ± 5.59	I13
IRAS 11095-0238	ULIRG	<1.20	6.08 ± 0.61	1.89 ± 0.19	1.22 ± 0.24	<0.90	⋯	⋯	FO16
Arp 299 B = NGC 3690_W[a]	LIRG	5.52 ± 1.11	103.80 ± 2.71	54.42 ± 0.98	47.71 ± 1.79	28.90 ± 3.78	204.00 ± 11.63	228.80 ± 6.27	I10
Arp 299 A = NGC 3690_E[b]	LIRG	5.06 ± 0.79	237.40 ± 2.65	57.05 ± 0.98	61.61 ± 2.04	16.07 ± 14.29	271.90 ± 22.72	267.00 ± 18.23	I10
NGC 4151	S1	84.80 ± 5.51	134.00 ± 5.84	214.50 ± 11.20	71.00 ± 5.05	244.00 ± 9.07	68.50 ± 5.90	135.00 ± 3.77	FO16
IRAS 12112+0305	ULIRG	0.47 ± 0.11	14.0 ± 0.14	3.70 ± 0.04	5.40 ± 0.16	<1.1	10.0 ± 0.5	⋯	I10, V09
NGC 4194	LIRG	9.15 ± 0.53	175.70 ± 1.40	56.20 ± 0.60	71.26 ± 0.91	25.10 ± 1.85	157.40 ± 8.53	185.50 ± 3.99	I13
NGC 4214-reg.1	Dwarf	56.80 ± 2.10	89.80 ± 2.20	187.00 ± 1.40	117.80 ± 2.00	<9.78	187.10 ± 2.70	⋯	C15
NGC 4536	H II	0.95 ± 0.20	35.46 ± 0.39	6.11 ± 0.06	16.34 ± 0.91	1.72 ± 0.25	100.48 ± 4.53	114.02 ± 1.53	FO16
NGC 4631	H II	1.39 ± 0.42	45.92 ± 0.71	10.15 ± 0.13	39.69 ± 2.12	<1.47	85.16 ± 0.76	114.74 ± 1.89	FO16
NGC 4945	S	⋯	698.40 ± 60.40	68.10 ± 2.27	⋯	28.35 ± 1.39	359.60 ± 20.40	732.80 ± 7.84	FO16
NGC 5033	S2	2.83 ± 0.20	13.26 ± 0.18	5.08 ± 0.15	14.88 ± 0.50	5.08 ± 0.51	17.38 ± 0.85	45.35 ± 1.52	FO16
IRAS 13120-5453	ULIRG	0.50 ± 0.10	150.00 ± 15.00	18.46 ± 1.85	19.18 ± 1.92	6.42 ± 1.28	60.64 ± 6.06	107.10 ± 10.70	FO16
Cen A = NGC 5128	S2	14.01 ± 3.55	189.10 ± 17.50	148.00 ± 6.08	48.50 ± 2.75	129.00 ± 7.05	148.80 ± 10.20	285.40 ± 8.86	FO16
M83-nucleus	H II	3.31 ± 0.23	503.33 ± 19.88	29.30 ± 0.77	227.66 ± 16.51	5.75 ± 1.08	263.50 ± 9.21	391.40 ± 8.55	FO16
NGC 5253	Dwarf	541. ± 211.	121.1 ± 59.6	656. ± 39.	261. ± 124.	9.80 ± 2.41	626. ± 398.	329. ± 231.	FO16
Mrk 273	S2	9.58 ± 0.96	41.90 ± 4.19	33.57 ± 3.36	13.35 ± 1.33	56.36 ± 5.64	42.56 ± 4.26	14.66 ± 2.90	FO16
IC 4329A	S1	29.10 ± 1.32	27.60 ± 0.73	57.00 ± 0.97	15.00 ± 1.44	117.00 ± 1.42	16.00 ± 2.19	32.50 ± 3.06	FO16
Mrk 463E	S1h	29.86 ± 2.99	9.25 ± 0.92	40.78 ± 4.08	15.85 ± 1.59	69.17 ± 6.92	15.50 ± 1.55	29.79 ± 2.98	FO16
Circinus	S1h	123.20 ± 53.20	393.00 ± 67.50	385.40 ± 29.90	194.50 ± 26.20	897.50 ± 48.90	594.40 ± 89.20	729.90 ± 51.70	FO16
NGC 5506	S1h	73.50 ± 1.56	85.10 ± 1.43	153.70 ± 1.10	58.60 ± 7.79	226.20 ± 4.00	91.70 ± 24.40	137.00 ± 6.92	FO16
NGC 6240	LIN	2.68 ± 0.27	171.00 ± 17.10	60.60 ± 6.10	17.10 ± 1.71	26.75 ± 2.67	38.11 ± 3.81	265.90 ± 26.60	FO16
IRAS 17208-0014	ULIRG	<0.4	38.0 ± 0.38	7.90 ± 0.16	7.30 ± 0.22	<3.2	<13.0	60.0 ± 1.2	V09
3C 405	S2	16.20 ± 0.70	21.70 ± 0.70	47.90 ± 0.50	24.20 ± 0.60	78.50 ± 0.70	29.00 ± 1.00	⋯	FO16
IRAS 20551-4250	ULIRG	<1.28	13.49 ± 0.95	2.73 ± 0.61	6.74 ± 0.43	<4.18	9.98 ± 4.49	23.30 ± 8.81	I13
NGC 7130 = IC 5135	S2	5.27 ± 0.84	79.30 ± 0.93	29.40 ± 0.77	19.60 ± 0.33	19.70 ± 0.84	48.20 ± 2.59	93.90 ± 4.90	FO16
NGC 7172	S2	5.87 ± 0.61	33.00 ± 1.01	17.10 ± 0.68	11.90 ± 1.00	45.40 ± 0.48	26.90 ± 1.51	59.30 ± 2.42	FO16

Table 3
(Continued)

Name	Type	$F_{[S\ IV]10.5\mu m}$ (10^{-17} W m^{-2})	$F_{[Ne\ II]12.8\mu m}$ (10^{-17} W m^{-2})	$F_{[Ne\ III]15.5\mu m}$ (10^{-17} W m^{-2})	$F_{[S\ III]18.7\mu m}$ (10^{-17} W m^{-2})	$F_{[O\ IV]25.9\mu m}$ (10^{-17} W m^{-2})	$F_{[S\ III]33.5\mu m}$ (10^{-17} W m^{-2})	$F_{[Si\ II]34.8\mu m}$ (10^{-17} W m^{-2})	Refs.
(1)	(2)	(3)	(4)	(5)	(6)	(7)	(8)	(9)	(10)
NGC 7314	S1h	15.90 ± 0.53	8.08 ± 0.39	23.20 ± 0.53	9.97 ± 0.71	67.00 ± 0.41	15.00 ± 1.71	14.20 ± 1.76	FO16
NGC 7469	S1	9.00 ± 0.79	191.00 ± 2.70	35.80 ± 0.75	75.40 ± 4.52	34.00 ± 3.80	63.60 ± 9.21	194.00 ± 19.10	FO16
NGC 7582	S1h	21.30 ± 1.43	322.00 ± 6.41	105.00 ± 2.05	87.30 ± 1.99	262.00 ± 5.54	244.00 ± 7.85	⋯	FO16
IRAS 23128-5919	ULIRG	4.80 ± 0.28	32.12 ± 0.45	21.72 ± 0.46	24.64 ± 1.70	14.97 ± 2.47	19.35 ± 2.28	34.03 ± 7.47	I13

Notes. From left to right, the table columns show the (1) object name; (2) galaxy type (dwarf galaxy, Seyfert, starburst (H II), and ULIRG); (3), (4), (5), (6), (7), (8), (9) fluxes of the given mid-IR fine-structure lines, in units of 10^{-17} W m^{-2}, from the following references: (10): FO16: Fernández-Ontiveros et al. (2016) and references therein; I13: Inami et al. (2013); C15: Cormier et al. (2015); D06: Dale et al. (2006): fluxes averaged over $\sim 23'' \times 15''$ and listed in units of 10^{-9} Wm^{-2} sr^{-1}; A07: Armus et al. (2007); V09: Veilleux et al. (2009); I10: Imanishi et al. (2010).
[a] $11^h28^m31\overset{s}{.}0\ 58^d33^m43$.
[b] $11^h28^m33\overset{s}{.}7\ 58^d33^m49$.

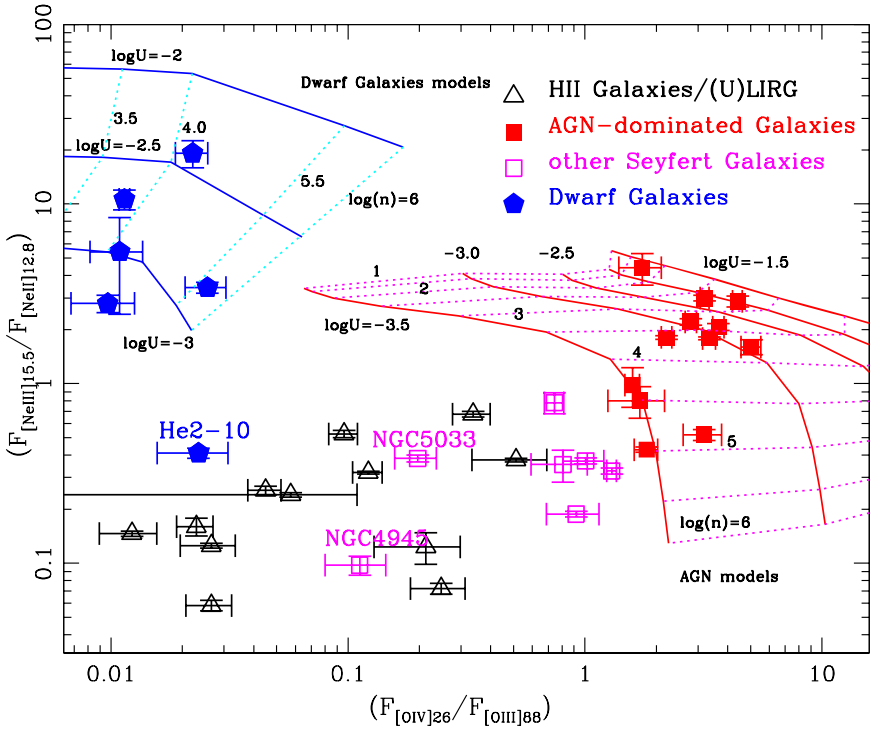

Figure 2. [Ne III] 15.5 μm/[Ne II] 12.8 μm line ratio vs. the [O IV] 25.9 μm/[O III] 88 μm line ratio, the so-called IR BPT diagram (Fernández-Ontiveros et al. 2016), showing the separation between the galaxy types: on the right, AGN; on the bottom left, starburst/H II region galaxies and ULIRGs; and on the upper-left part, the dwarf galaxies, characterized by low metallicity. The two Seyfert galaxies NGC 4945 and NGC 5033 have line ratios more typical of H II region galaxies, and the dwarf galaxy He 2–10 is also similar to them. A grid of AGN photoionization models (models A in Section 4) spans the parameter values of $1.0 < \log(n) < 6.0$ and $-3.5 < \log(U) < -1.5$. Similarly, a grid of low-metallicity starburst galaxy models (models A in Section 4 with a metallicity of $Z = 0.004$ (1/5 $Z_\odot$)) spans the ranges of $3.5 < \log(n) < 6.0$ and $-3.0 < \log(U) < -2.0$.

Table 4
Observed Properties of Other Galaxies Observed by SOFIA in the [O III]52 μm Line

Name	R.A.	Decl.	z	Type	$12 + \log(O/H)$	$F_{[O\ III]52\mu m}$ [10^{-17} W m^{-2}]	$F_{[O\ III]88\mu m}$ [10^{-17} W m^{-2}]	Notes	References
(1)	(2)	(3)	(4)	(5)	(6)	(7)	(8)	(9)	(10)
IC 342	$03^h46^m48\overset{s}{.}5$	$+68^d05^m47^s$	0.000103	H II	8.71 ± 0.01	98.21 ± 18.99	171.14 ± 7.92	† #	
NGC 2366	$07^h28^m55\overset{s}{.}6$	$+69^d13^m05^s$	0.000267	Dwarf	7.64 ± 0.03	155.84 ± 39.85	226.00 ± 1.00	† #	M13, C15
UGC 5189	$09^h42^m54\overset{s}{.}7$	$+09^d29^m01^s$	0.010720	H II	8.29 ± 0.07	30.75 ± 4.45	⋯	† #	PT07
NGC 3077	$10^h03^m19\overset{s}{.}1$	$+68^d44^m02^s$	0.000047	H II	8.60 ± 0.01	745.65 ± 112.98	⋯	† #	C04
Mrk 1271	$10^h56^m09\overset{s}{.}1$	$+06^d10^m22^s$	0.003380	H II	7.99 ± 0.04	<12[a]	⋯	† #	I98
Pox 4	$11^h51^m11\overset{s}{.}6$	$-20^d36^m02^s$	0.011970	H II	7.97 ± 0.06	46.85 ± 6.44	⋯	† #	K96
Mrk 193	$11^h55^m28\overset{s}{.}3$	$+57^d39^m52^s$	0.017202	H II	7.79 ± 0.27	<12[b]	⋯	† #	I94
NGC 4536	$12^h34^m27\overset{s}{.}1$	$+02^d11^m17^s$	0.006031	H II	8.83 ± 0.01	136.90 ± 29.26	166.61 ± 7.63	† #	
NGC 4670	$12^h45^m17\overset{s}{.}1$	$+27^d07^m31^s$	0.003566	Dwarf	8.47 ± 0.02	38.17 ± 4.2	⋯	† #	

Notes. From left to right, the table columns show the (1) object name; (2), (3) 2MASS coordinates; (4) NED redshift (z); (5) galaxy type: dwarf galaxy, Seyfert, starburst (H II), luminous IR galaxy (LIRG) or ultraluminous IR galaxy (ULIRG); (6) optical metallicity; (7), (8) line fluxes, in units of 10^{-17} W m^{-2}, of the lines: $F_{[N\ III]57\mu m}$ $F_{[O\ III]88\mu m}$; (9) origin of far-IR spectroscopy: †: $F_{[O\ III]52\mu m}$ from SOFIA FIFI-LS; #: SOFIA data reduced in this work; the $F_{[O\ III]88\mu m}$ line fluxes are from Herschel-PACS (Fernández-Ontiveros et al. 2016, and references therein); (10) reference for the metallicity data: M13: Madden et al. (2013); C15: Cormier et al. (2015); PT07: Pilyugin & Thuan (2007); C04: Calzetti et al. (2004); I98: Izotov & Thuan (1998); K96: Kobulnicky & Skillman (1996); I94: Izotov et al. (1994).
[a] 3σ upper limit, very noisy line profile.
[b] 3σ upper limit, line profile not consistent with the expected line width of $\sim$300 kms^{-1}.

galaxy with stellar populations of different ages. They produced the spectra for five different stellar metallicities ($Z_\star = 0.05\ Z_\odot$, 0.2 $Z_\odot$, 0.4 $Z_\odot$, $Z_\odot$, and 2 $Z_\odot$) available for the Geneva evolutionary tracks (Meynet et al. 1994). AGN photoionization models follow the prescription of starburst models, but with an ionizing spectrum with a broken power law with an index $\alpha = -1.4$ ($S_\nu \propto \nu^\alpha$) between 10 μm and 50 keV, $\alpha = 2.5$ for $\lambda > 10\ \mu$m and $\alpha = -2.0$ for $E > 50$ keV. The range of the ionization parameters, $\log U = -3.0$ to -1.6, is that of typical AGNs. The remaining input parameters of the model (gas-phase abundances, stopping criteria, gas density range, dust grains, etc.) are the same as what we used for the starburst models.

Two independent abundance determinations were obtained for both the O/H and N/O ratios using the optical and the infrared nebular lines. The estimates were derived with the HII-

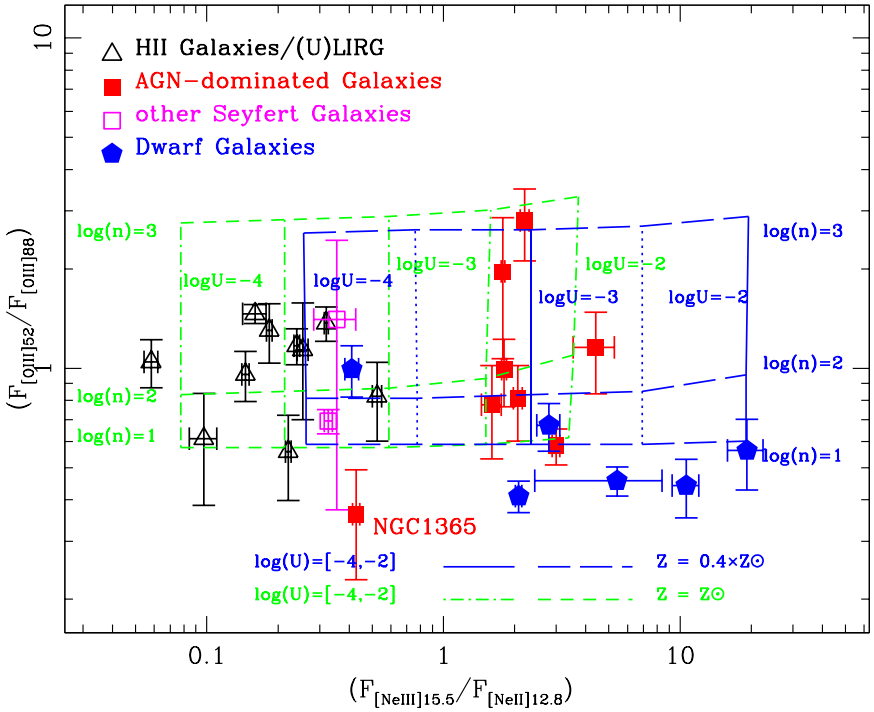

Figure 3. Ionization–density diagram made with the [O III] 52 μm/88 μm ratio vs. the [Ne III] 15.5 μm/[Ne II] 12.8 μm ratio. The grid of models (models B in Section 4) represents starburst models with density $\log(n) = [1, 3]$ and ionization potential of $\log(U) = [-2, -4]$. Two types of abundances have been assumed: solar (grid with density as short-dashed line and ionization parameter as dotted–dashed line) and subsolar with $Z = 0.4 \times Z_{\odot}$ (grid with density as long-dashed line and ionization parameter as a solid line). The effect of subsolar abundances shifts the models to the right and intersects a low-metallicity dwarf galaxy.

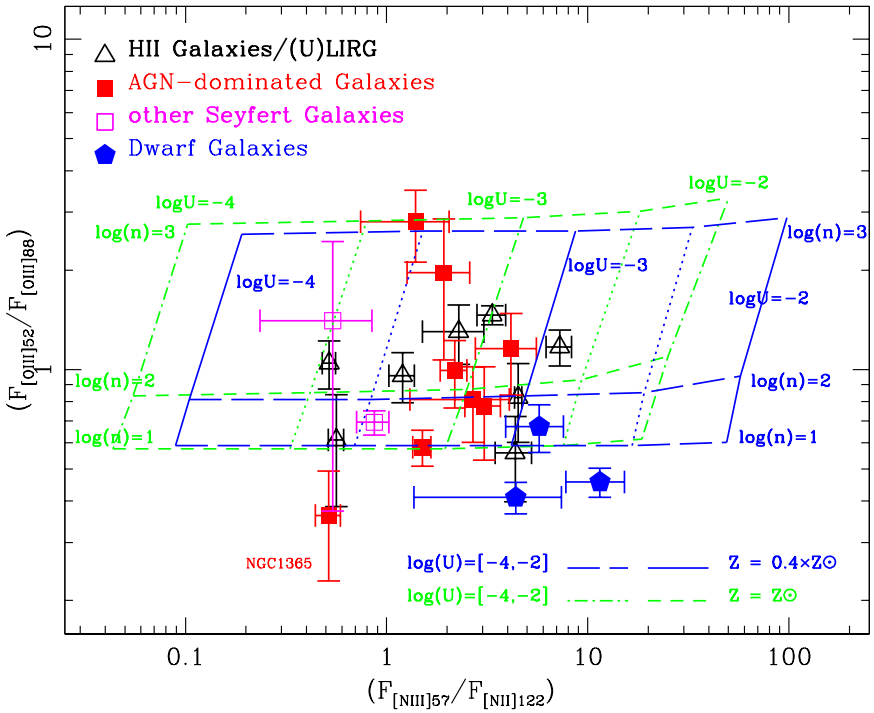

Figure 4. Ionization–density diagram made with the [O III]52 μm/88 μm ratio vs. the [N III] 57 μm/[N II] 122 μm ratio. The models are the same as in Figure 3, again with the two types of abundances: solar and subsolar ($Z = 0.4 \times Z_{\odot}$).

CHI-MISTRY (hereafter HCM; Pérez-Montero 2014) and the HII-CHI-MISTRY-IR codes[11] (HCM-IR; Fernández-Ontiveros et al. 2021). Both are based on the same grid of photoionization models (hereafter models C), computed using CLOUDY (Ferland et al. 2017), adopting simple stellar population models from POPSTAR as the incident radiation field (Mollá et al. 2009). The models sample a wide range in oxygen abundance ($6.9 < 12 + \log(\mathrm{O/H}) < 9.1$), nitrogen abundance ($-2.0 < \log(\mathrm{N/O}) < 0.0$), and ionization parameter ($-4.0 < \log U < -1.5$), assuming a filling factor of 0.1 and a constant

[11] Available at https://www.iaa.csic.es/~epm/HII-CHI-mistry.html.

electron density of $n_e = 100\,\mathrm{cm}^{-3}$. To compute the optical-based abundances for AGNs, we used photoionization models assuming a power-law ionizing continuum ($F_\nu \propto \nu^{\alpha_{OX}}$; $\alpha_{OX} = -1.2$) and $n_e = 500\,\mathrm{cm}^{-3}$ (see Pérez-Montero et al. 2019). We refer to Fernández-Ontiveros et al. (2021) for a comparison of the predicted emission-line ratios with the observed ones for a sample of star-forming galaxies, showing that the range of variations of the main emission-line ratios of this sample are within the ranges covered by the models.

HCM and HCM-IR perform a Bayesian-like calculation of the 12 + log(O/H) and the N/O abundances and the ionization parameter by comparing the optical (reddening-corrected) and infrared nebular lines, respectively, with the predicted values in the grids of photoionization models. The abundance determination does not rely on a single best-fit model, but it is instead based on the Bayesian calculation where all the models contribute to the computation of the abundances. The estimated abundance and its associated uncertainty are then computed from the weighted grid of models, as discussed in Fernández-Ontiveros et al. (2021). The photoionization models provide abundance estimates consistent with the direct method—based on the detection of auroral nebular lines in the optical range—within a scatter of 0.1 dex and 0.2 dex, respectively (Pérez-Montero 2014; Fernández-Ontiveros et al. 2021).

For the case of AGNs, the abundance determinations could not be obtained using HCM-IR due to the lack of hydrogen recombination-line measurements in the mid-IR. Humphreys α is the brightest recombination line in the range covered by Spitzer/IRS in the high-spectral-resolution mode (9.9–37.1 μm); however, it is a weak line ($\sim$1/100th of Hβ), and thus it is not reported in most of the works discussed in Section 2.2, where these spectra were analyzed. Therefore, IR-based 12 + log(O/H) determinations are not available for the AGNs in our sample. In this regard, IR-based abundance determinations for AGNs will be addressed in a forthcoming work (B. Pérez-Díaz et al. 2022, in preparation). Nevertheless, a robust estimate of the N/O abundance ratio can be obtained from the [O III] 52 μm, 88 μm, and [N III] 57 μm lines, due to the similar ionization structure of these two elements. For this purpose, we define the N3O3 parameter, based on the relative intensities of the nitrogen and oxygen lines in the far-IR:

$$\mathrm{N3O3} = \log\left(\frac{\mathrm{I}([\mathrm{N\ III}]_{57\mu\mathrm{m}})}{\mathrm{I}([\mathrm{O\ III}]_{52\mu\mathrm{m}}) + \mathrm{I}([\mathrm{O\ III}]_{88\mu\mathrm{m}})}\right). \quad (4)$$

This parameter was used by Peng et al. (2021) and Fernández-Ontiveros et al. (2021) for the derivation of the N/O relative abundances in star-forming galaxies and can be also be applied to the case of NLRs in AGNs, due to its very low dependence on the excitation conditions of the ionized gas. This is due to the similar ionization structure of the oxygen and nitrogen elements in the nebula. To this aim, we analyzed the predicted values of N3O3 for the grid of AGN photoionization models described in Pérez-Montero et al. (2019). For the input ionizing source, we adopted a double-peak power law with index $\alpha_{UV} = -1.5$, also considering different values for $\alpha_{OX} = -0.8$ and -1.2, with an electron density of $n_e = 500\,\mathrm{cm}^{-3}$, sampling the same range in metallicity, ionization parameter, and N/O mentioned earlier. The N3O3 parameter presents a very tight relation with the N/O abundances in star-forming regions (Fernández-Ontiveros et al. 2021; Peng et al. 2021). This is also true under harder radiation fields in AGNs, as shown by the linear sequence of AGN models at a fixed 12 + log(O/H) = 8.8 and $\alpha_{OX} = -1.2$ in Appendix B. Thus, a robust linear relation between these parameters can be extracted. The linear fit to the whole set of models for this value of α_{OX} has a correlation coefficient of 0.91 and results in the following expression:

$$\log(\mathrm{N/O}) = (0.97 \pm 0.01) \times \mathrm{N3O3} - (0.01 \pm 0.01). \quad (5)$$

Additionally, the analysis for the model grid with $\alpha_{OX} = -0.8$ leads to similar results within the typical observational errors.

5. Results

We discuss the results of the abundance determination through both the optical and IR spectral lines. We use in the following a few diagrams showing various IR line ratios as a function of the metallicity. We also compare both the (O/H) and (N/O) abundance determinations using the two methods.

5.1. Far-IR Line Ratios as a Function of Gas-phase Metallicity

Following the work of Nagao et al. (2011) and Pereira-Santaella et al. (2017), we present for the H II region/ULIRG galaxies and the dwarf galaxies of our sample, in Figure 5, the ratio of (2.2 × [O III]88 μm + [O III] 52 μm)/[N III] 57 μm as a function of the gas-phase metallicity as measured in the optical and expressed in terms of 12 + log(O/H). The starburst galaxy photoionization models are taken from Pereira-Santaella et al. (2017) (models B in Section 4) and include values of the ionization parameter $\log(U) = -2$, -3, and -4 and electron densities with $\log(n_e/\mathrm{cm}^{-3}) = [1, 3]$. These models follow the same relation between N/O and O/H derived by Pilyugin et al. (2014), adopted in Pereira-Santaella et al. (2017), and reported in Equation (2) of this latter study.

We also show in the same figure (solid line (in green)) a photoionization model (from models C in Section 4) with $\log(U) = -3$, $\log(n_e/\mathrm{cm}^{-3}) = 2$, and $\log(\mathrm{N/O}) = -1.54$ for metallicities of $[12 + \log(\mathrm{O/H})] < 8.09$ and $\log(\mathrm{N/O}) = 4.21 + 1.47 \times \log(\mathrm{O/H})$ for metallicities of $[12 + \log(\mathrm{O/H})] > 8.09$, which corresponds to the Pilyugin et al. (2014) relation between N and O, as well as (green broken lines) the effect of increasing and decreasing, in the lower and upper curves, respectively, the log(N/O) by 0.35 dex. It appears clear from this plot that, to fit most galaxies, a N/O ratio of a factor of $\sim$2 higher or lower than the solar value is needed. As anticipated in Section 4, the different photoionization models shown in Figure 5 do agree well, and a slight discrepancy only appears for high metallicities $[12 + \log(\mathrm{O/H})] \gtrsim 8.7$. This shows that only minor differences are present in the N/O abundances using the constant-pressure models in Pereira-Santaella et al. (2017) and the constant-density models used in HCM and HCM-IR.

The same line ratio is presented for AGNs, also including the dwarf galaxies for comparison, in Figure 6. Here the photoionization model grid (models B in Section 4) includes models with ionization parameter $\sim -2.8 < \log(U) < -1.6$ and densities of $\sim 2.0 < \log(n_e) < 6.0$ cm^{-3}. Also, in this case, the large scatter of the points around the given models could be due to a different value of the N/O ratio.

In Figure 7, we show the ratio [O III] 88.3 μm/[N III] 57.2 μm versus the metallicity for all galaxies of the sample, including the H II region/ULIRG galaxies, dwarf galaxies, and AGNs. Here both starburst and AGN models (models B in Section 4) are included, and the intrinsic spread of the models

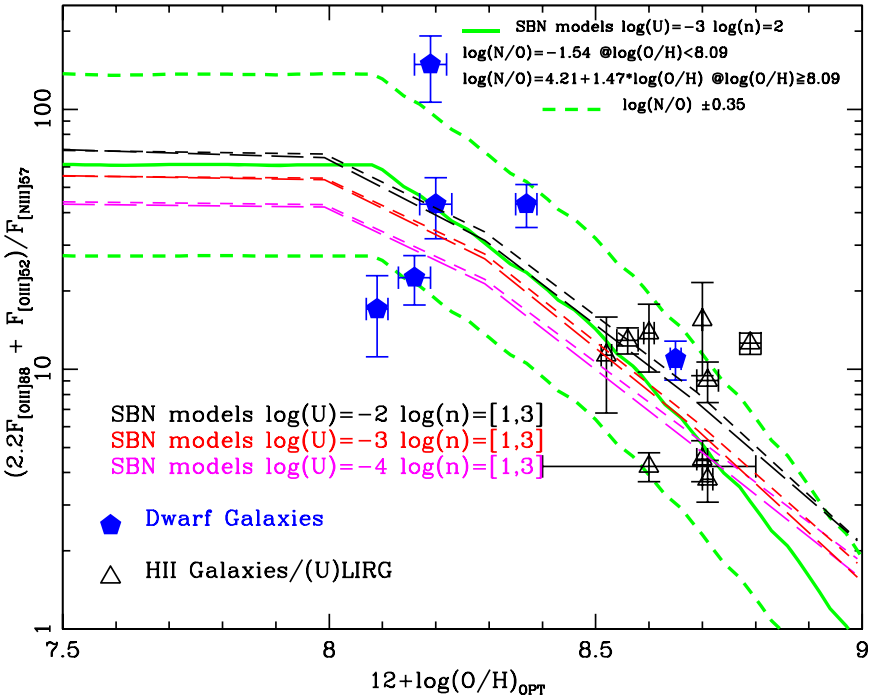

Figure 5. Ratio of (2.2 × [O III] 88 μm + [O III] 52 μm)/[N III] 57 μm as a function of the gas-phase metallicity for the H II region/ULIRG galaxies and the dwarf galaxies of our sample. The photoionization models (models B in Section 4) are taken from Pereira-Santaella et al. (2017) and include values of the ionization parameter $\log(U) = -2$, -3, and -4 from the top to the bottom and densities with $\log(n_e/\mathrm{cm}^{-3}) = [1, 3]$. The solid line (in green) represents a photoionization model (models C in Section 4) with $\log(U) = -3$, $\log(n_e/\mathrm{cm}^{-3}) = 2$, and $\log(\mathrm{N/O}) = -1.54$ for metallicities of $[12 + \log(\mathrm{O/H})] < 8.09$ and $\log(\mathrm{N/O}) = 4.21 + 1.47 \times \log(\mathrm{O/H})$ for metallicities of $[12 + \log(\mathrm{O/H})] > 8.09$. The two broken lines (in green) show the effect of increasing and decreasing, respectively, the log(N/O) by 0.35 dex.

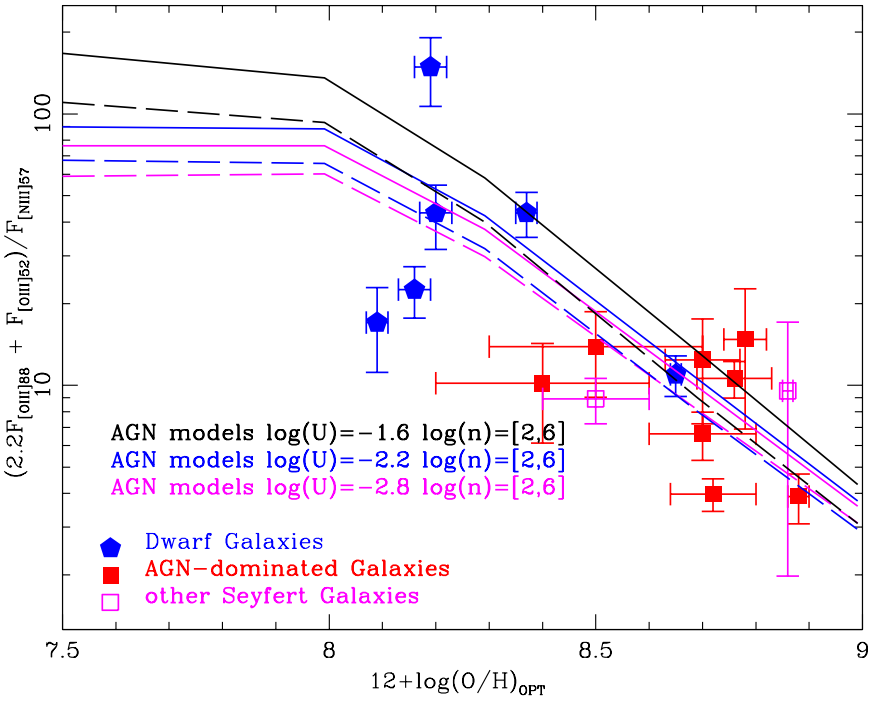

Figure 6. Same as Figure 5, but with the AGN observations and the relative photoionization models (models B in Section 4) from Pereira-Santaella et al. (2017). The dwarf-galaxy observations have been included for comparison.

is larger than that in the case of the previous composite line ratio. Also, these photoionization models follow the same relation between N/O and O/H derived by Pilyugin et al. (2014) and adopted in Pereira-Santaella et al. (2017).

Figure 8 shows the [O III] 88 μm/[N II] 122 μm ratio as a function of the gas-phase metallicity for all galaxies of our sample, compared to the starburst photoionization models (models B in Section 4). Also these photoionization models

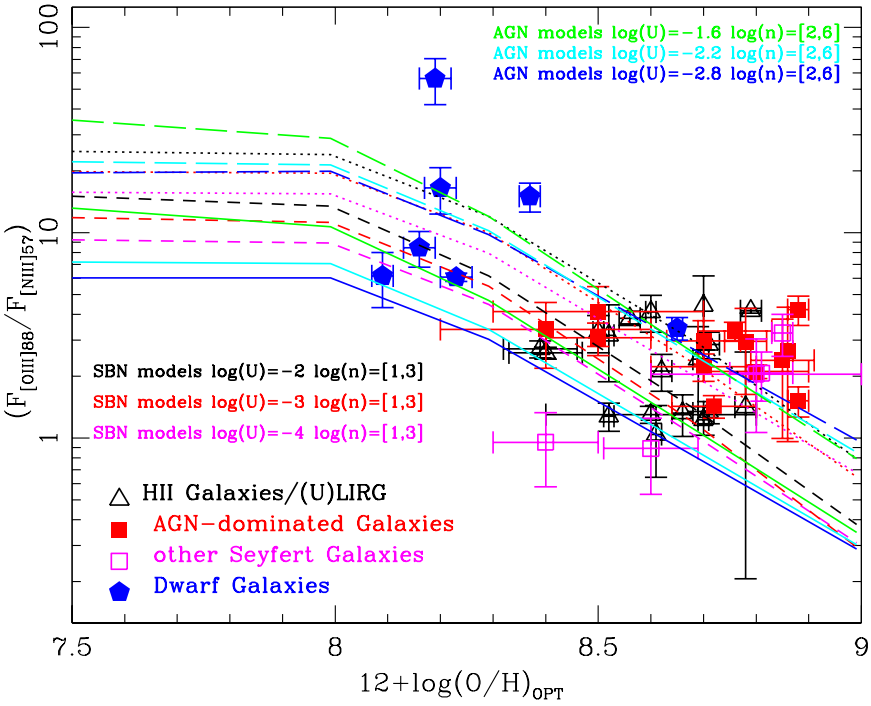

Figure 7. Ratio of [O III] 88 μm/[N III] 57 μm as a function of the gas-phase metallicity. The photoionization models (models B in Section 4) are taken from Pereira-Santaella et al. (2017) and include values of the ionization potential $\log(U) = -2$, -3, and -4 from the top to the bottom and densities with $\log(n_e/\mathrm{cm}^{-3}) = [1, 3]$ for the starburst models and ionization potential $\log(U) = -1.6$, -2.2, and -2.8 from the top to the bottom and densities with $\log(n_e/\mathrm{cm}^{-3}) = [2, 6]$ for the AGN models.

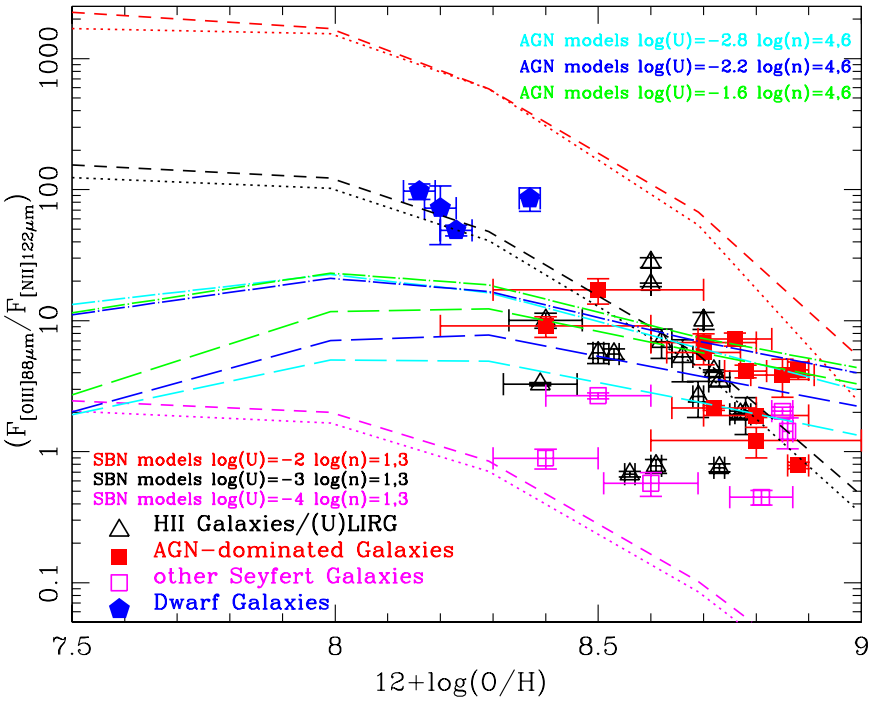

Figure 8. Ratio of [O III] 88 μm/[N II] 122 μm as a function of the gas-phase metallicity. The photoionization models (models B in Section 4) are taken from Pereira-Santaella et al. (2017) and include values of ionization potential $\log(U) = -2$, -3, and -4 from the top to the bottom and densities with $\log(n_e/\mathrm{cm}^{-3}) = [1,3]$ for the starburst models and ionization potential $\log(U) = -1.6$, -2.2, and -2.8 from the top to the bottom and densities with $\log(n_e/\mathrm{cm}^{-3}) = [4, 6]$ for the AGN models.

follow the same relation between N/O and O/H derived by Pilyugin et al. (2014) and adopted in Pereira-Santaella et al. (2017). One can see from this figure a large spread in the models produced by different ionization parameters. In other words, the determination of the metallicity from a given line ratio is only reliable if we can measure the ionization parameter through other line ratios.

In Figure 9 we show the [O III] 88 μm/[N II] 122 μm line ratio as a function of the [N III] 57 μm/[N II] 122 μm line ratio for both solar and subsolar abundances (models B in Section 4). As before, the subsolar value has been set to $Z = 0.4 \times Z_{\odot}$. We can see from this diagram that only a few objects (4/5 dwarf galaxies) need subsolar abundances. We also notice that we can read out from the vertical axis a precise

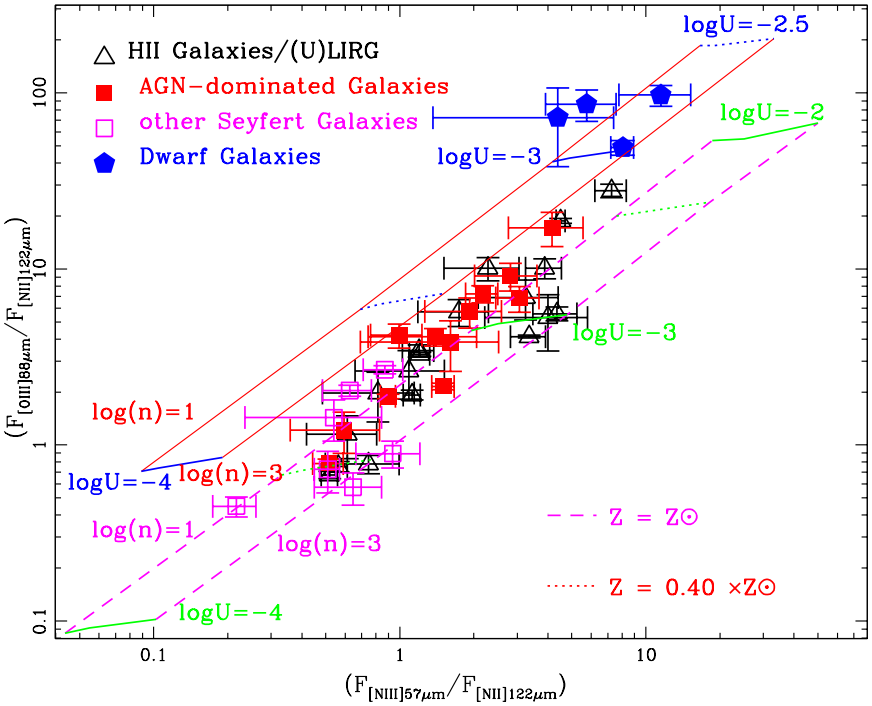

Figure 9. Ratio of [O III] 88 μm/[N II] 122 μm as a function of the [N III] 57 μm/[N II] 122 μm line ratio. The photoionization models (models B in Section 4) are taken from Pereira-Santaella et al. (2017) and include values of the ionization potential $\log(U) = -2$, -3, -3.5, and -4 from the top to the bottom and densities with $\log(n) = [1, 3]$ for the starburst models. For comparison, the AGN data points have also been included. The lower grid assumes solar abundances, while the upper grid indicates models with a subsolar metallicity of $Z = 0.4 \times Z_{\odot}$.

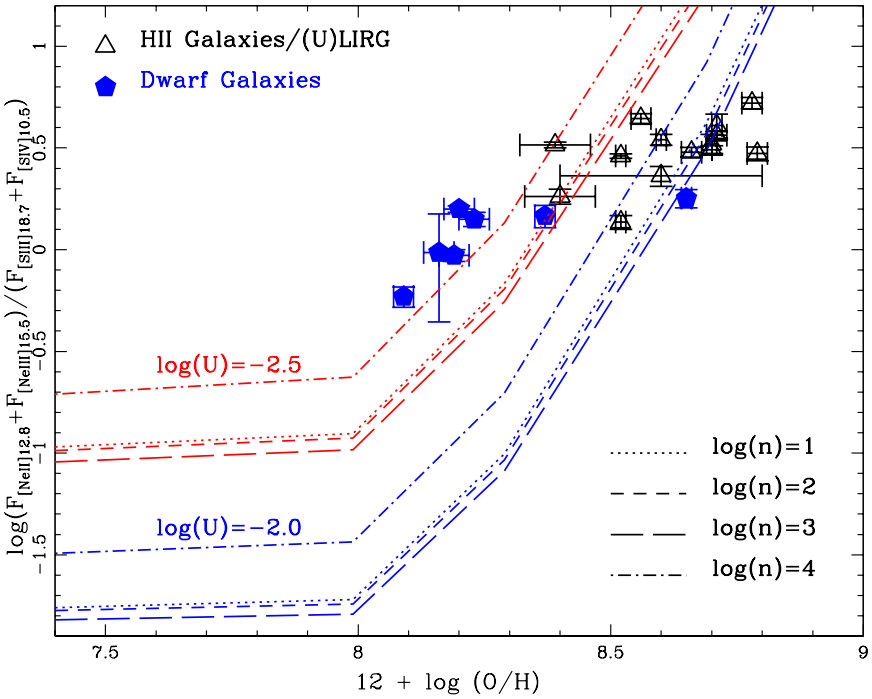

Figure 10. Logarithm of the observed ratio of the sum of ([Ne II] 12.8 μm + [Ne III] 15.5 μm) to the sum of ([S III] 18.7 μm + [S IV] 10.5 μm) vs. the optical metallicity (Fernández-Ontiveros et al. 2016) for the starburst and dwarf galaxies of our sample. Two sets of CLOUDY photoionization models (models A in Section 4) with $\log(U) = -2.5$ (upper models) and $\log(U) = -2.0$ (lower models) are compared to the data, assuming sulfur depletion at $[12 + \log(\mathrm{O/H})] > 8$ for electron densities in the range of $\log(n) = [1, 4]$.

estimate of the ionization parameter: assuming, e.g., solar abundances, we can associate a value of $\log(U) = -4$ at [O III] 88 μm/[N II] 122 μm = 0.1, a value of $\log(U) = -3$ for a ratio $\sim$5, and a value of $\log(U) = -2$ at a ratio of $\gtrsim$50. It follows that observations of the three far-IR lines of [N III] 57 μm, [O III] 88 μm, and [N II] 122 μm can break the degeneracy due to the ionization parameter. In other words, placing an observed galaxy in this diagram will give an estimate of the ionization parameter and therefore make possible an estimate of the metallicity through the use of the diagram in Figure 8.

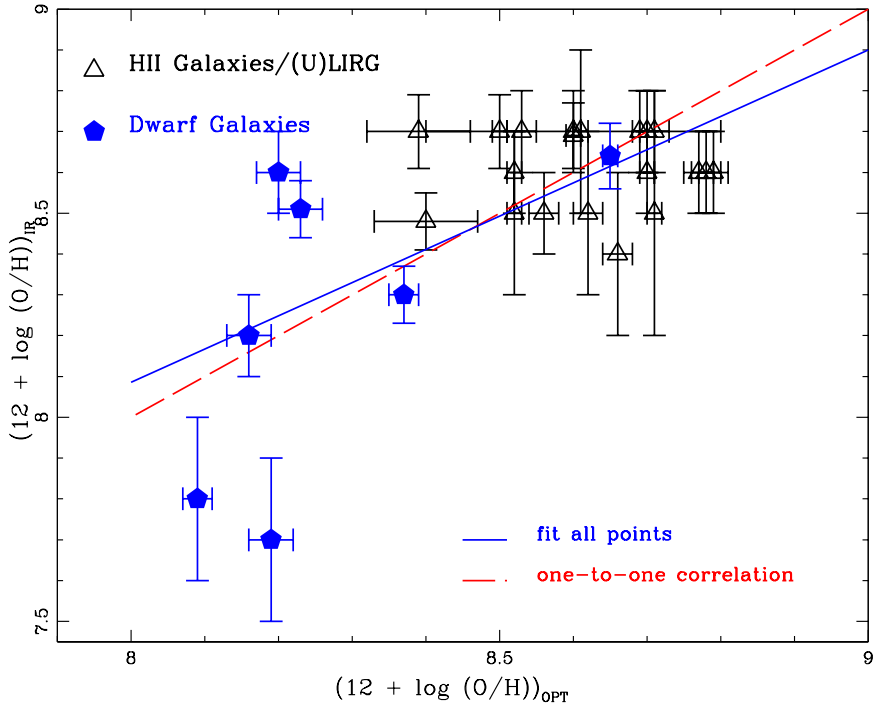

Figure 11. Metallicity derived from IR lines, using the method from Fernández-Ontiveros et al. (2021), is compared to the metallicity computed from the optical lines using Pérez-Montero (2014). The dashed line shows the one-to-one correlation, while the solid line gives the fit $y = (0.89 \pm 0.15) \cdot x - (0.83 \pm 1.32)$ ($\chi^2 = 0.53$, $R = 0.77$).

5.2. Mid-IR Line Ratios as a Function of Gas-phase Metallicity

Following the work presented in Fernández-Ontiveros et al. (2016, 2017), we have also considered the ratio of ([Ne II] 12.8 μm + [Ne III] 15.5 μm) to ([S III] 18.7 μm + [S IV] 10.5 μm), which, as a first approximation, is equal to the total neon to total sulfur ratio if one excludes active galaxies, which can also ionize the [Ne V] IR fine-structure lines. In Figure 10 this ratio is shown as a function of the metallicity computed from the optical emission lines. Starburst galaxies photoionization models (models A in Section 4) with an ionization parameter of $-2.5 < \log(U) < -2.0$ and densities $1 < \log(n_e/\mathrm{cm}^{-3}) < 4$ have been included. These models assume sulfur depletion for [12 + log(O/H)]> 8. It appears evident from this figure that there is a correlation between the neon to sulfur ratio, measured by the $Ne_{23}S_{34}$ index, and the gas-phase metallicity. In conclusion, we confirm the results of Fernández-Ontiveros et al. (2016, 2017) that these line fluxes can be used to measure metallicity. This is important also because the upcoming mission of the James Webb Space Telescope (JWST; Gardner et al. 2006) will be able to detect these IR fine-structure lines in the local universe and at low redshift ($z \leqslant 0.8$).

5.3. Metallicities from Optical Lines versus IR Lines

In Figure 11 the metallicity derived from IR lines, using the method from Fernández-Ontiveros et al. (2021), is compared to the metallicity computed from the optical lines using Pérez-Montero (2014). A fit to the data is shown in the figure, which agrees within the errors with the one-to-one correlation. It follows that from the data of our sample of galaxies, there is no significant difference between the determination of the metallicity through optical lines and that through IR lines.

5.4. N/O Ratio from Optical Lines versus IR Lines

In Figure 12 the $(N/O)_{IR}$ ratio derived from IR lines, using the method of Fernández-Ontiveros et al. (2021), is compared to the $(N/O)_{OPT}$ ratio computed from the optical lines using the work of Pérez-Montero (2014). It appears from this comparison that the N/O ratio computed from the IR lines is on average lower than that derived from optical lines, especially at high values of N/O (N/O > −1). The solar value measured with optical lines $(N/O)_{OPT}(\odot) \sim 0.24$ corresponds, according to the fit, to an IR-determined value of $(N/O)_{IR}(\odot) \sim 0.12$, i.e., a factor of 2 lower. A least-squares fit to the data results in a slope much flatter than the value of $\alpha = 1$. Considering all star-forming galaxies, i.e., the H II galaxies and ULIRGs together with the dwarf galaxies, the fit gives a slope of $\alpha = 0.68 \pm 0.12$, while using all the galaxies of our sample the slope is $\alpha = 0.52 \pm 0.10$.

5.5. N/O Abundance Ratio

In Figure 13 the N/O ratio, computed from the IR emission lines using the method developed by Fernández-Ontiveros et al. (2021) and reported in Table 5, is plotted as a function of the metallicity, computed also from the IR emission lines.

In Figure 14 the N/O ratio, computed from the optical emission lines using the method developed by Pérez-Montero (2014) and reported in Table 5, is plotted as a function of the metallicity, computed also from the optical emission lines.

If we compare the average value of the $\log(N/O)_{IR} = -0.73 \pm 0.34$ (Figure 13) with the average value of the $\log(N/O)_{OPT} = -0.94 \pm 0.30$ (Figure 14), we see a large difference of ∼0.2 dex.

In the following sections we study the possible dependence of Δ(N/O) on ionization, density, and extinction.

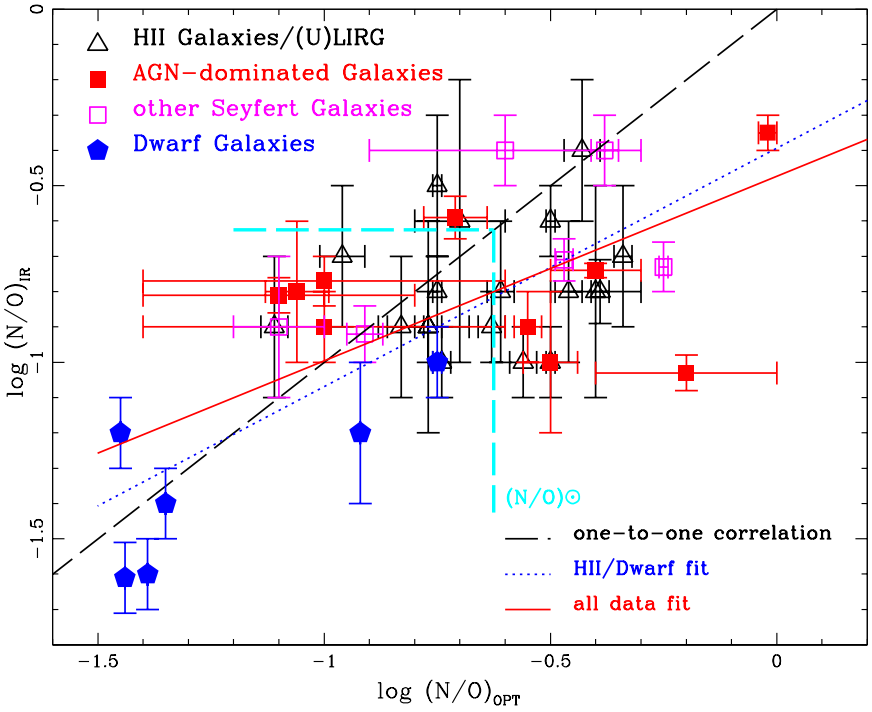

Figure 12. N/O ratio derived from IR, using the method from IR lines of Fernández-Ontiveros et al. (2021), is compared to the N/O ratio computed from the optical lines using Pérez-Montero (2014). The dashed line shows the one-to-one correlation, while the dotted line gives the fit for H II/ULIRG and dwarf galaxies: $y = (0.68 \pm 0.12) \cdot x - (0.39 \pm 0.10)(\chi^2 = 0.93, R = 0.76)$. A fit to all the data gives (shown as a solid line) $y = (0.52 \pm 0.10) \cdot x - (0.47 \pm 0.08)(\chi^2 = 1.84, R = 0.64)$. The solar value of $(N/O) = 0.24$ is also indicated.

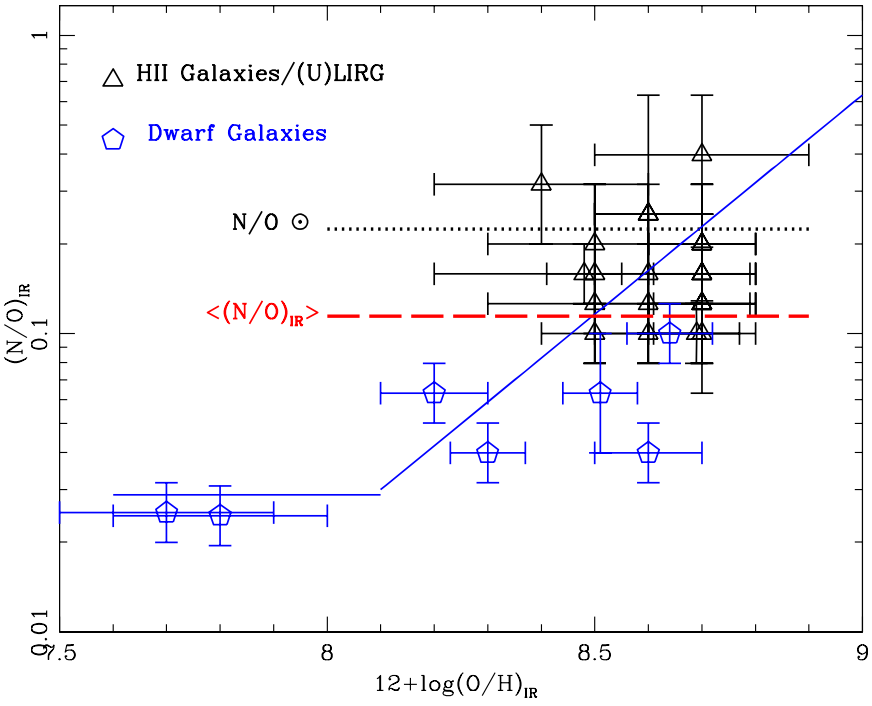

Figure 13. N/O ratio computed from IR emission lines vs. the metallicity similarly computed. The solar value of $N/O = 0.24$ has been indicated as well as the average value of $\log(N/O)_{IR} = -0.94 \pm 0.30$. The Pilyugin et al. (2014) relation between N and O is shown as a solid line, for comparison, which assumes $\log(N/O) = -1.54$ for $[12 + \log(O/H)] < 8.1$ and $\log(N/O) = 4.21 + 1.47 \times [\log(O/H)]$ for $[12 + \log(O/H)] > 8.1$.

5.5.1. Δ(N/O) versus Ionization

Figure 15 shows the logarithmic difference between the N/O ratio computed from IR emission lines $(N/O)_{IR}$ and the N/O from optical lines $(N/O)_{OPT}$ (hereafter $\Delta(N/O) = (N/O)_{OPT} - (N/O)_{IR}$) versus the [Ne III] 15.5 μm/[Ne II] 12.8 μm line ratio. In this diagram a slight decreasing trend is present, which could be due to the higher $\Delta(N/O)$ values in H II galaxies and (U)LIRGs, albeit the correlation is not statistically significant. Dwarf galaxies are on average consistent with an equal value for the (N/O), and

Table 5
Observed Properties of the Local Galaxy Sample: Coordinates, Types, and Metallicities

Name (1)	R.A. (2)	Decl. (3)	z (4)	Type (5)	$12 + \log(O/H)$ (6)	$\log(N/O)$ (7)	References. (8)	$12 + \log(O/H)_{IR}$ (9)	$\log(N/O)_{IR}$ (10)
Haro 11	$00^h36^m52\overset{s}{.}5$	$-33^d33^m17^s$	0.020598	Dwarf	8.23 ± 0.03	-0.92	M13, C19	8.51 ± 0.07	-1.2 ± 0.2
NGC 253	$00^h47^m33\overset{s}{.}1$	$-25^d17^m19^s$	0.000811	H II	8.61 ± 0.01	-0.43 ± 0.04	TW	8.7 ± 0.2	-0.4 ± 0.2
MCG+12-02-001	$00^h54^m03\overset{s}{.}6$	$+73^d05^m12^s$	0.015698	LIRG	8.7	...	AH10	8.7 ± 0.1	-1.0 ± 0.1
NGC 1068	$02^h42^m40\overset{s}{.}7$	$-00^d00^m48^s$	0.003793	S1h	8.60 ± 0.06	-0.02 ± 0.02	TW	...	-0.35 ± 0.05
NGC 1365	$03^h33^m36\overset{s}{.}4$	$-36^d08^m26^s$	0.005457	S1	8.88 ± 0.02	...	TW	...	-0.3 ± 0.05
NGC 1569	$04^h30^m49\overset{s}{.}0$	$+64^d50^m53^s$	−0.000347	Dwarf	8.19 ± 0.03	−1.39	M13, C19	7.7 ± 0.2	-1.6 ± 0.1
NGC 1614	$04^h34^m00\overset{s}{.}0$	$-08^d34^m45^s$	0.015938	H II	8.60 ± 0.01	-0.56 ± 0.03	TW	8.69 ± 0.08	-1.0 ± 0.1
NGC 1808	$05^h07^m42\overset{s}{.}3$	$-37^d30^m46^s$	0.003319	H II	8.71 ± 0.01	-0.4 ± 0.1	TW	8.5 ± 0.3	-0.8 ± 0.3
II Zw 40	$05^h55^m42\overset{s}{.}6$	$+03^d23^m32^s$	0.002632	Dwarf	8.09 ± 0.02	−1.44	M13, C19	7.7 ± 0.2	-1.3 ± -0.2
Mrk 3	$06^h15^m36\overset{s}{.}4$	$+71^d02^m15^s$	0.013509	S1h	8.69 ± 0.07	-0.55 ± 0.03	TW	...	-0.9 ± 0.1
NGC 2146	$06^h18^m37\overset{s}{.}8$	$+78^d21^m25^s$	0.002979	LIRG	8.71 ± 0.02	-0.77 ± 0.03	TW	8.7 ± 0.1	-0.9 ± 0.1
NGC 2366	$07^h28^m55\overset{s}{.}6$	$+69^d13^m05^s$	0.000267	Dwarf	7.64 ± 0.03	...	M13		...
He 2–10	$08^h36^m15\overset{s}{.}2$	$-26^d24^m34^s$	0.002912	Dwarf	8.65 ± 0.01	-0.75 ± 0.01	TW	8.64 ± 0.08	-1.0 ± 0.1
IRAS 08572+3915	$09^h00^m25\overset{s}{.}4$	$+39^d03^m54^s$	0.05835	ULIRG	8.62 ± 0.02	-0.96 ± 0.05	TW	8.5 ± 0.2	-0.7 ± 0.2
UGC 5101	$09^h35^m51\overset{s}{.}6$	$+61^d21^m11^s$	0.01615	ULIRG	8.78 ± 0.02	-0.7 ± 0.1	TW	8.6 ± 0.1	-0.6 ± 0.4
M82	$09^h55^m52\overset{s}{.}7$	$+69^d40^m46^s$	0.00068	H II	8.70 ± 0.01	-0.46 ± 0.03	TW	8.6 ± 0.1	-0.8 ± 0.2
NGC 3256	$10^h27^m51\overset{s}{.}3$	$-43^d54^m13^s$	0.00935	H II	8.39 ± 0.07	-0.39 ± 0.02	TW	8.70 ± 0.09	-0.80 ± 0.09
Haro 3	$10^h45^m22\overset{s}{.}4$	$+55^d57^m38^s$	0.003149	Dwarf	8.37 ± 0.02	−1.35	M13, C19	8.30 ± 0.07	-1.4 ± 0.1
IRAS 10565+2448	$10^h59^m18\overset{s}{.}2$	$+24^d32^m34^s$	0.04310	ULIRG	8.77 ± 0.02	-0.50 ± 0.01	TW	8.6 ± 0.1	-0.6 ± 0.1
IRAS 11095–0238	$11^h12^m03\overset{s}{.}4$	$-02^d54^m23^s$	0.106634	ULIRG	8.53 ± 0.02	-0.77 ± 0.09	TW	8.7 ± 0.1	-0.9 ± 0.3
Arp 299 A = IC 694	$11^h28^m33\overset{s}{.}7$	$58^d33^m49^s$	0.01041	LIRG	8.56 ± 0.02	-0.74 ± 0.02	TW	8.5 ± 0.1	-1.0 ± 0.1
Arp 299 B+C = NGC 3690	$11^h28^m31\overset{s}{.}0$	$58^d33^m43^s$	0.01022	LIRG	8.79 ± 0.02	-0.50 ± 0.01	TW	8.6 ± 0.1	-1.0 ± 0.1
NGC 4151	$12^h10^m32\overset{s}{.}6$	$+39^d24^m21^s$	0.003319	S1	8.5 ± 0.1	-0.71 ± 0.07	TW	...	-0.59 ± 0.06
IRAS 12112+0305	$12^h13^m46\overset{s}{.}0$	$+02^d48^m38^s$	0.073317	ULIRG	8.66 ± 0.02	-0.75 ± 0.01	TW	8.4 ± 0.2	-0.5 ± 0.2
NGC 4194	$12^h14^m09\overset{s}{.}5$	$+54^d31^m37^s$	0.008342	LIRG	8.52 ± 0.01	-0.63 ± 0.03	TW	8.5 ± 0.2	-0.9 ± 0.1
NGC 4214-reg.1	$12^h15^m39\overset{s}{.}3$	$+36^d19^m37^s$	0.00097	Dwarf	8.20 ± 0.03	...	M13	8.6 ± 0.1	-1.4 ± 0.1
NGC 4631	$12^h42^m07\overset{s}{.}8$	$+32^d32^m35^s$	0.002021	H II	8.52 ± 0.01	-1.11 ± 0.03	TW	8.69 ± 0.07	-0.8 ± -0.3
NGC 4945	$13^h05^m27\overset{s}{.}5$	$-49^d28^m06^s$	0.00188	S2	...	...		8.5 ± 0.4	-0.6 ± 0.2
NGC 5033	$13^h13^m27\overset{s}{.}5$	$+36^d35^m38^s$	0.00292	S2	8.85 ± 0.07	-0.25 ± 0.01	TW	...	-0.73 ± 0.07
IRAS 13120–5453	$13^h15^m06\overset{s}{.}4$	$-55^d09^m23^s$	0.03076	ULIRG	...	...		8.7 ± 0.1	-0.7 ± 0.2
Cen A = NGC 5128	$13^h25^m27\overset{s}{.}6$	$-43^d01^m09^s$	0.00183	S2	8.85 ± 0.02	-0.91 ± 0.04	TW	...	-0.92 ± 0.08
M83	$13^h37^m00\overset{s}{.}9$	$-29^d51^m56^s$	0.001711	H II	8.6 ± 0.2	-0.34 ± 0.02	TW	8.7 ± 0.1	-0.7 ± 0.2
NGC 5253	$13^h39^m56\overset{s}{.}0$	$-31^d38^m24^s$	0.001358	Dwarf	8.16 ± 0.03	−1.45	M13, C19	8.2 ± 0.1	-1.2 ± 0.1
Mrk 273	$13^h44^m42\overset{s}{.}1$	$+55^d53^m13^s$	0.03778	S2	8.85 ± 0.06	-1.06 ± 0.07	TW	...	-0.8 ± 0.2
IC 4329A	$13^h49^m19\overset{s}{.}3$	$-30^d18^m34^s$	0.016054	S1	8.4 ± 0.2	-1.0 ± 0.4	TW	...	-0.77 ± 0.07
Mrk 463E	$13^h56^m02\overset{s}{.}9$	$+18^d22^m18^s$	0.05035	S1h	8.5 ± 0.2	-1.0 ± 0.4	TW	...	-0.9 ± 0.1
Circinus	$14^h13^m09\overset{s}{.}9$	$-65^d20^m21^s$	0.00145	S1h	8.8 ± 0.1	-0.4 ± 0.1	TW	...	-0.74 ± 0.02

Table 5
(Continued)

Name (1)	R.A. (2)	Decl. (3)	z (4)	Type (5)	$12 + \log(O/H)$ (6)	$\log(N/O)$ (7)	References. (8)	$12 + \log(O/H)_{IR}$ (9)	$\log(N/O)_{IR}$ (10)
NGC 5506	$14^h13^m14\overset{s}{.}9$	$-03^d12^m28^s$	0.006181	S1h	8.76 ± 0.07	-1.1 ± 0.3	TW	...	-0.81 ± 0.05
NGC 6240	$16^h52^m58\overset{s}{.}9$	$+02^d24^m04^s$	0.02448	LIN	8.85 ± 0.01	-1.1 ± 0.1	TW	...	-0.9 ± 0.2
IRAS 17208–0014	$17^h23^m21\overset{s}{.}9$	-00 d17^m01^s	0.042810	ULIRG	8.69 ± 0.01	-0.61 ± 0.03	TW	8.7 ± 0.1	-0.8 ± 0.2
3C 405 = Cyg A	$19^h59^m28\overset{s}{.}3$	$+40^d44^m02^s$	0.056075	S2	8.78 ± 0.04	-0.50 ± 0.06	TW	...	-1.0 ± 0.2
IRAS 20551–4250	$20^h58^m26\overset{s}{.}8$	$-42^d39^m00^s$	0.042996	ULIRG	8.50 ± 0.01	-0.83 ± 0.05	TW	8.70 ± 0.09	-0.9 ± 0.2
NGC 7130 = IC 5135	$21^h48^m19\overset{s}{.}5$	$-34^d57^{mm}05^s$	0.01615	S2	8.60 ± 0.09	-0.6 ± 0.3	TW	...	-0.4 ± 0.1
NGC 7172	$22^h02^m01\overset{s}{.}9$	$-31^d52^m11^s$	0.00868	S2	8.8 ± 0.2	...	TW	...	-0.7 ± 0.1
NGC 7314	$22^h35^m46\overset{s}{.}2$	$-26^d03^m02^s$	0.004763	S1h	8.88 ± 0.02	-0.2 ± 0.2	TW	...	-1.03 ± 0.05
NGC 7469	$23^h03^m15\overset{s}{.}6$	$+08^d52^m26^s$	0.01632	S1	8.4 ± 0.1	-0.38 ± 0.03	TW	...	-0.4 ± 0.1
IRAS 23128–5919	$23^h15^m46\overset{s}{.}8$	$-59^d03^m16^s$	0.04460	ULIRG	8.40 ± 0.07	-0.75 ± 0.01	TW	8.48 ± 0.07	-0.8 ± 0.1
NGC 7582	$23^h18^m23\overset{s}{.}7$	$-42^d22^m14^s$	0.005254	S1h	8.5 ± 0.1	-0.47 ± 0.02	TW	...	-0.71 ± 0.06

Notes. From left to right, the table columns show the (1) object name; (2), (3) 2MASS coordinates; (4) NED redshift (z); (5) galaxy type: dwarf, Seyfert, starburst (H II), luminous IR galaxy (LIRG) or ultraluminous IR galaxy (ULIRG); (6), (7) oxygen abundance and nitrogen-to-oxygen relative abundance determined from optical nebular lines; (8) references for the optical abundances: AH10: Alonso-Herrero et al. (2010), C19: Cormier et al. (2019), M13: Madden et al. (2013), TW: this work; (9) oxygen abundance and nitrogen-to-oxygen relative abundance determined from IR nebular lines using HCM-IR (Fernández-Ontiveros et al. 2021).

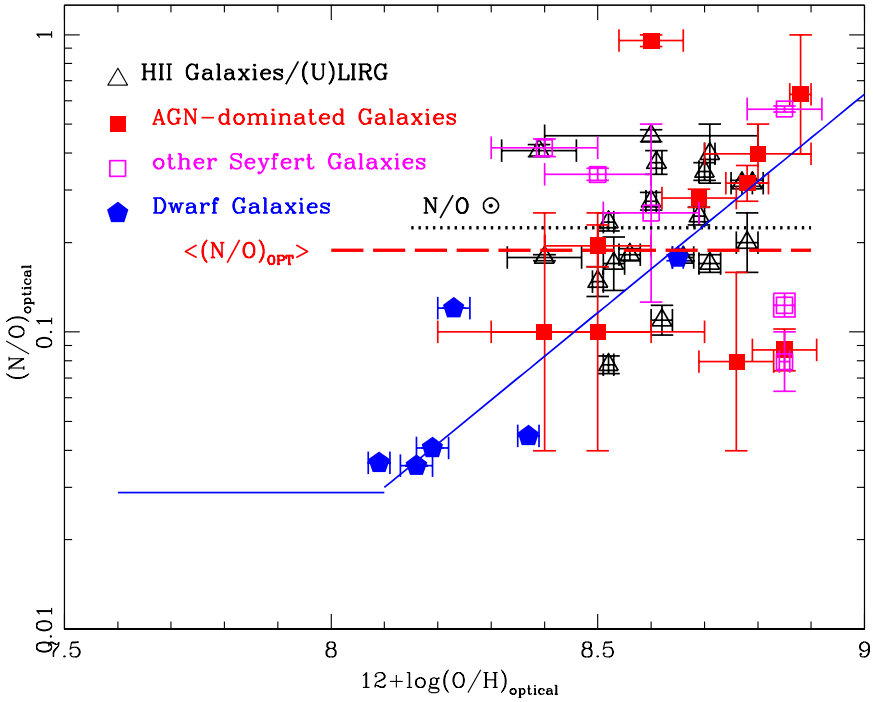

Figure 14. N/O ratio computed from optical emission lines vs. the metallicity similarly computed. The solar value of N/O = 0.24 has been indicated as the average value of $\log(N/O)_{OPT} = -0.73 \pm 0.34$. The Pilyugin et al. (2014) relation between N and O is shown as a solid line, for comparison, as given in the caption of Figure 13.

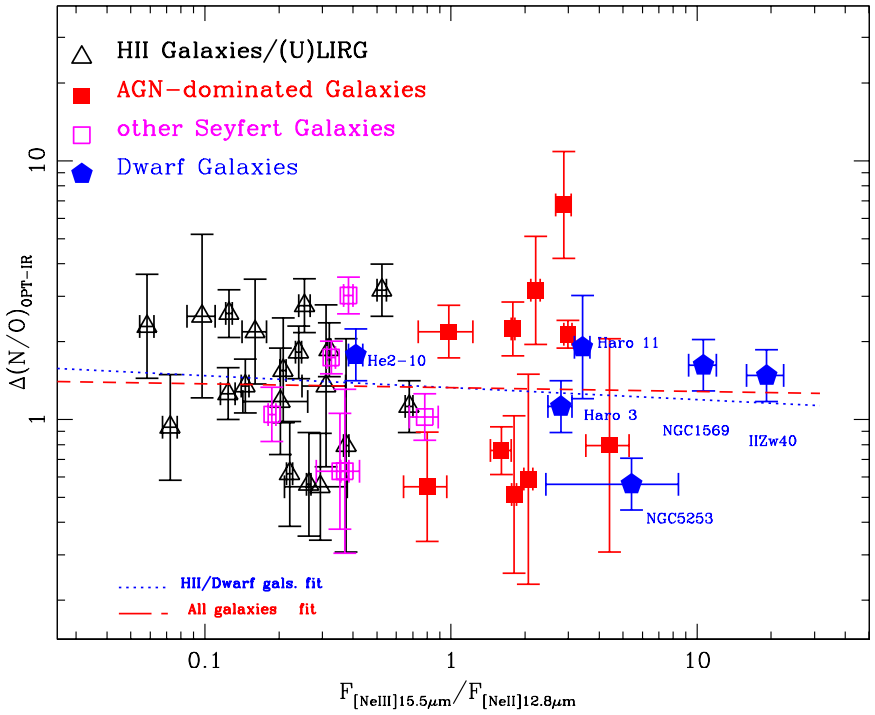

Figure 15. Logarithmic difference between the N/O ratio computed from the IR emission lines and the N/O from optical lines vs. the [Ne III] 15.5 μm/[Ne II] 12.8 μm line ratio, which measures the gas ionization. The dotted line gives the fit for H II/ULIRG and dwarf galaxies: $y = (-0.05 \pm 0.07) \cdot x + (0.12 \pm 0.05)$ ($\chi^2 = 1.19$, $R = -0.14$). A fit to all the data gives (shown as a dashed line) $y = (-0.01 \pm 0.07) \cdot x + (0.12 \pm 0.05)$($\chi^2 = 2.92$, $R = -0.03$).

Seyfert galaxies have a high dispersion. A similar diagram is shown in Figure 16, using the [N III] 57 μm/[N II] 122 μm line ratio; however, the scatter is larger here, due to the lower ionization potential of these lines, which result in a larger confusion along the horizontal axis.

We also present in Figure 17 the Δ(N/O) plotted as a function of the [O IV]26 μm/[O III]88 μm line ratio, which covers the largest range in ionization and almost three orders of magnitude in line-ratio value from low-metallicity dwarf galaxies to AGNs. Also in this case the search for a correlation

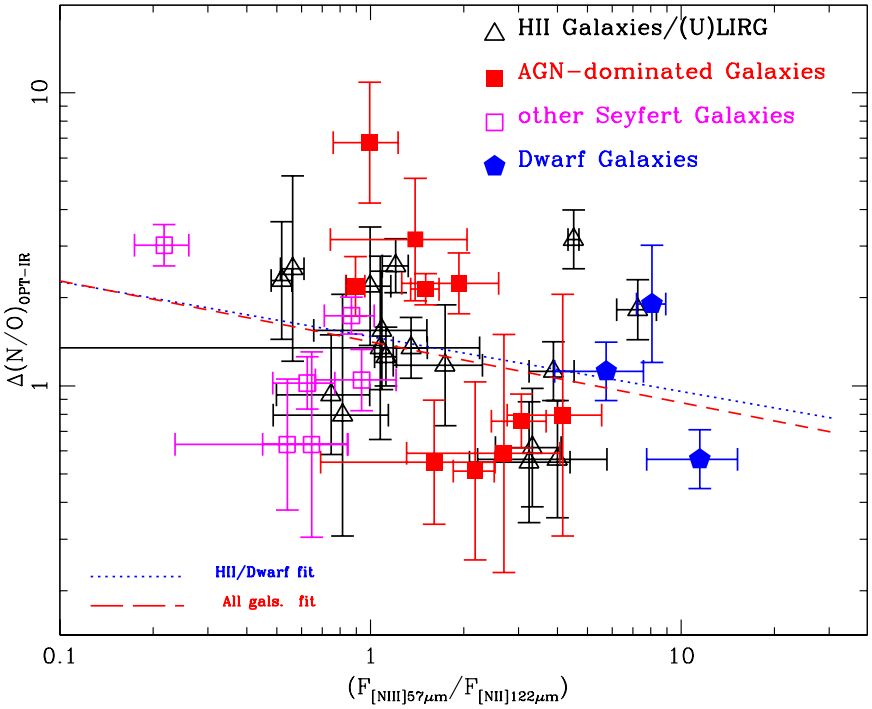

Figure 16. Logarithmic difference between the N/O ratio computed from IR emission lines and the N/O from optical lines vs. the [N III] 57 μm/[N II] 122 μm line ratio, which measures the gas ionization. The dotted line gives the fit for H II/ULIRG and dwarf galaxies: $y = (-0.18 \pm 0.13) \cdot x + (0.16 \pm 0.06)(\chi^2 = 0.97, R = -0.31)$. A fit to all the data gives (shown as a dashed line) $y = (-0.21 \pm 0.12) \cdot x + (0.15 \pm 0.05)(\chi^2 = 2.54, R = -0.29)$.

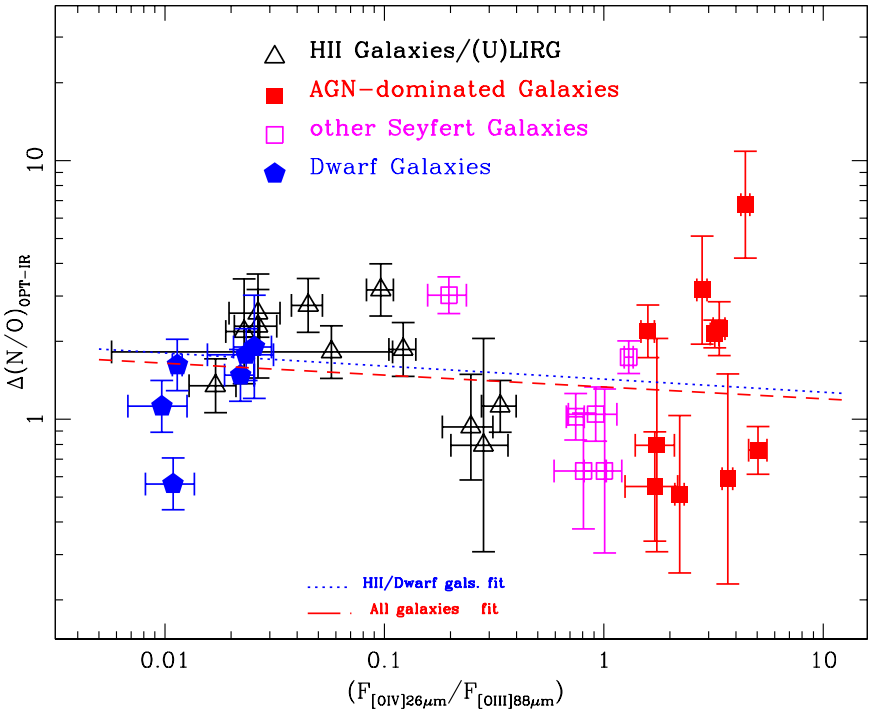

Figure 17. Logarithmic difference between the N/O ratio computed from IR emission lines and the N/O from optical lines vs. the [O IV] 26 μm/[O III] 8 μm line ratio, which measures the gas ionization. The dotted line gives the fit for H II/ULIRG and dwarf galaxies: $y = (-0.04 \pm 0.10) \cdot x + (0.14 \pm 0.15)(\chi^2 = 0.64, R = -0.10)$. A fit to all the data gives (shown as a dashed line) $y = (-0.05 \pm 0.05) \cdot x + (0.12 \pm 0.06)(\chi^2 = 2.36, R = -0.15)$.

fails because of the large spread of the data; however, a slight trend of increasing Δ(N/O) at low gas ionization remains for H II galaxies and (U)LIRGs.

5.5.2. Δ(N/O) versus Density

In Figure 18 we explore the dependence of Δ(N/O) on the electron density of the gas as measured from the optical [S II]

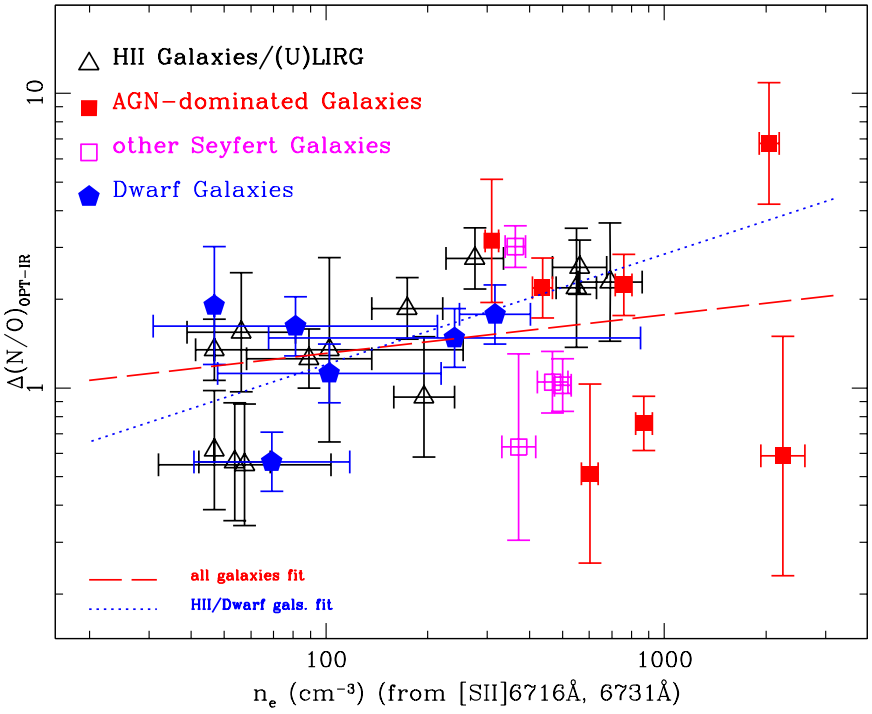

Figure 18. Logarithmic difference between the N/O ratio computed from IR emission lines and the N/O from optical lines vs. the electron density of the gas, as measured from the optical [S II] $\lambda\lambda$ 6716,6731 doublet. The dotted line gives the fit for H II/ULIRG and dwarf galaxies: $y = (0.37 \pm 0.10) \cdot x - (0.67 \pm 0.22)$ ($\chi^2 = 0.53$, $R = 0.66$). A fit to all the data gives (shown as a dashed line) $y = (0.13 \pm 0.09) \cdot x - (0.14 \pm 0.23)$($\chi^2 = 2.63$, $R = 0.25$).

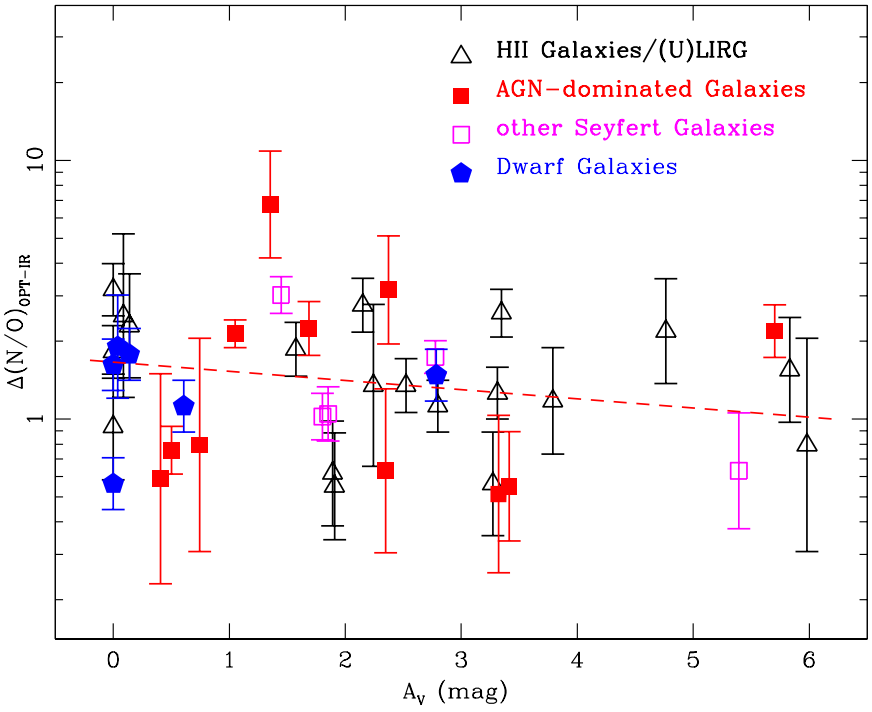

Figure 19. Logarithmic difference between the N/O ratio computed from IR emission lines and the N/O from optical lines vs. the galaxy extinction A_V in mag. The dashed line gives the fit all galaxies: $y = (-0.03 \pm 0.02) \cdot x + (0.22 \pm 0.07)$($\chi^2 = 3.51$, $- R = 0.21$).

$\lambda\lambda$6716, 6731 doublet. One can see from this figure that the star-forming galaxies (H II region/ULIRGs and dwarf galaxies) show an increasing correlation between the Δ(N/O) and the electron density, showing the highest value of Δ(N/O) for the highest densities. The inclusion of Seyfert galaxies breaks the correlation, probably due to the presence of gas in the NLR of these galaxies.

We refer to Appendix C for two similar diagrams of Δ(N/O) as a function of the electron density derived from the [S III] 18.7 μm and 33.5 μm lines and from the [O III] 52 μm and

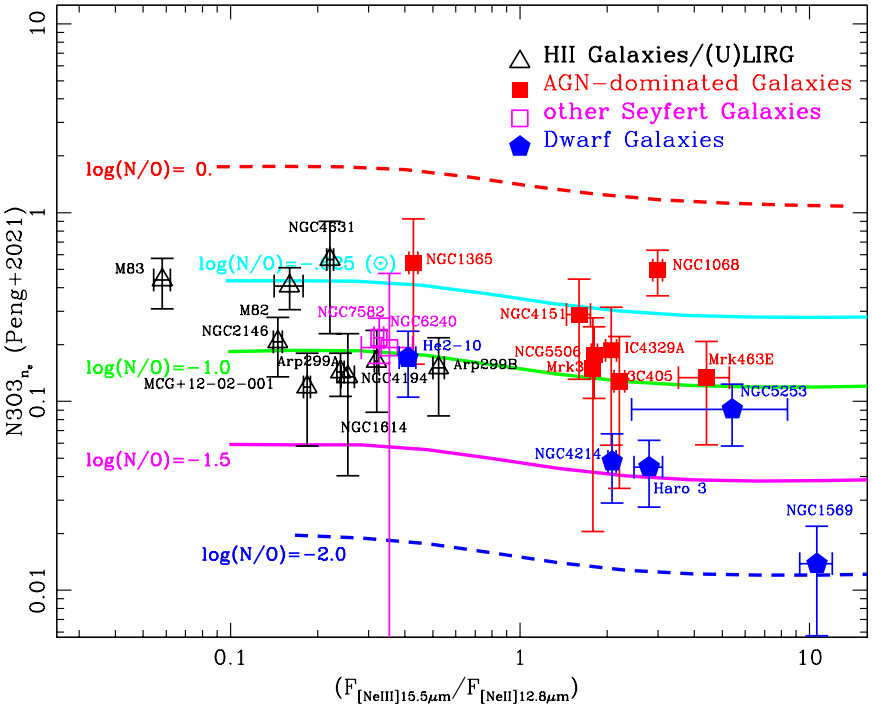

Figure 20. Density-corrected N3O3n_e (Peng et al. 2021) of the sample galaxies as a function of the [Ne III] 15.5 μm/[Ne II] 12.8 μm line ratio. The galaxies are divided into three classes, H II region galaxies/(U)LIRGs, Seyfert galaxies, and dwarf galaxies and are labeled with their names. The horizontal lines give the positions of constant N/O ratio as computed from photoionization models.

88 μm lines. Also using as density tracers the IR fine-structure lines of [S III] and [O III], we do not find any correlation between Δ(N/O) and electron density. This also demonstrates that there is no influence of the lower critical density of IR fine-structure lines as compared to the optical lines.

5.5.3. Δ(N/O) versus Extinction

We explored if the difference between the optical and IR determination of the (N/O) ratio could be due to an inaccurate extinction correction of the optical lines used to derive the optical (N/O) ratio. If this were the case, we would expect that a higher value of the Δ(N/O) value would originate in galaxies affected by higher dust extinction. In Figure 19 we have plotted the Δ(N/O) value as a function of the optical extinction A_V in magnitudes. It can be seen from the figure that no correlation is apparent, and the trend shows a decreasing Δ(N/O) value as a function of extinction. Therefore, we can rule out the hypothesis that this is due to extinction.

5.5.4. Density-corrected N/O Abundance Ratio

Recently, Peng et al. (2021) presented the results of the analysis of the SOFIA observations of the far-IR lines of [N III] 57 μm and [O III] 52 μm of eight galaxies, complemented by Herschel-PACS and Spitzer-IRS observations of [O III] 52 μm, [Ne II] 12.8 μm, and [Ne III] 15.5 μm, respectively. They show that the [N III] 57 μm/[O III] 52 μm line ratio, denoted N3O3, is a physically robust probe of N/O, insensitive to gas temperature, and only weakly dependent on electron density. They also use the observations of the two lines [O III] 52 μm and 88 μm to correct this ratio for the effects of density. We have therefore used this work to derive the density-corrected N3O3$_{n_e}$ ratio for our sample of galaxies and confirm our results with an independent method. The value of N3O3$_{n_e}$ was derived using Equations (2) and (4) of Peng et al. (2021). We present in Figure 20 the N3O3$_{n_e}$ ratio as a function of the [Ne III] 15.5 μm/[Ne II] 12.8 μm line ratio for each galaxy for which we have observations of the fine-structure lines of [O III] 52 and 88 μm, [N III] 57 μm, [Ne II] 12.8 μm, and [Ne III] 15.5 μm. In Figure 21 we show the same N3O3$_{n_e}$ ratio as a function of the [N III] 57 μm/[N II] 122 μm line ratio. Together with the data points of our sample of galaxies, we also show in these figures the lines of constant N/O ratio (log(N/O) = [−2, 0.]) analogously to Figure 3 of Peng et al. (2021). The lines at a fixed (N/O) ratio have been taken from CLOUDY photoionization models for stellar populations described in Section 4, adopting a solar O/H abundance, an ionization parameter in the range of log(U) = −4.0−1.5, and electron density fixed at the value of log(n_e) = 2.0 (cm^{-3}).

6. Discussion

One of the main results in this study is the difference found between optical and IR determinations of the N/O abundance in galaxies. Although the scatter in Figure 12 is relatively large, a systematic difference is observed for those galaxies with N/O abundances above $\gtrsim -0.6$ dex determined from the optical lines. These galaxies, including both star-forming galaxies and AGNs, show IR-based N/O abundances, which are about a factor of 2–3 lower when compared with the optical estimates, in agreement with the results obtained by Peng et al. (2021) for a sample of eight galaxies. This difference is in contrast with the overall agreement found between the optical and IR O/H abundance determinations in Figure 11. Optical and IR methods are consistent within ~0.2 dex scatter when O/H abundances are derived (Fernández-Ontiveros et al. 2021), but differ in the N/O values obtained.

Among the different possibilities to explain this discrepancy, we investigated three main scenarios that could affect the

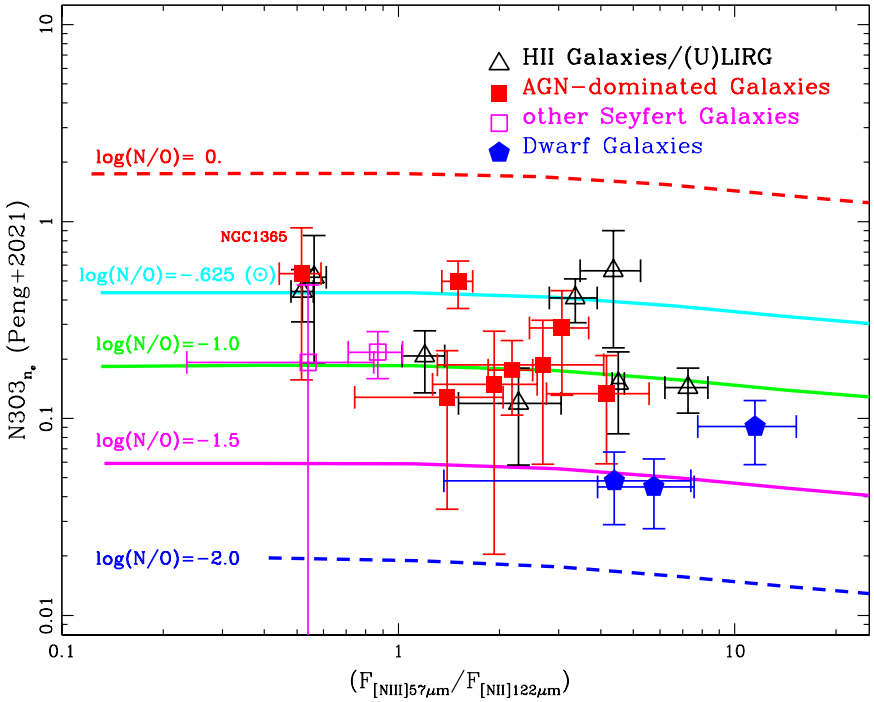

Figure 21. Density-corrected N3O3n_e (Peng et al. 2021) of the sample galaxies as a function of the [N III] 57 μm/[N II] 122 μm line ratio. The galaxies are divided into three classes, H II region galaxies/(U)LIRGs, Seyfert galaxies, and dwarf galaxies. The horizontal lines give the positions of constant N/O ratio as computed from photoionization models.

optical-line tracers: differences in the ionization structure, contamination by diffuse ionized gas (DIG; e.g., Vale Asari et al. 2019), and dust extinction. None of these hypotheses seem to explain the observed discrepancy. A difference in the ionization structure could result in lower N/O ratios for the IR tracers because these lines probe higher-ionization gas (O^{2+} and N^{2+}) located closer to massive stars, where the primary production of nitrogen could be prevalent, resulting in lower N/O when compared to the optical lines that trace lower-ionization gas (O^{+} and N^{+}) with a higher nitrogen enrichment from a secondary origin. However, Figures 15 and 16 show a flat distribution when the ratio between the N/O optical and IR estimates is compared with the strength of the radiation field traced by the [Ne III] 15.5 μm/[Ne II] 12.8 μm and [N III] 57 μm/[N II] 122 μm ratios, respectively. That is, star-forming galaxies with a strong radiation field (i.e., low-metallicity dwarf galaxies) are scattered around optical-to-IR N/O ratios of ∼1 in Figure 15, while solar-like starburst galaxies with the weakest radiation fields are tentatively shifted to ratios around ∼2.

An alternative explanation is the contamination by DIG affecting the optical lines in these galaxies. The presence of hot and low-density gas in the ISM was proposed by Peng et al. (2021) as a possible cause of the optical-to-IR discrepancy. In this scenario, the DIG contamination would be stronger for the lower-excitation species of O^{+} and N^{+}. As a matter of fact, the DIG emission can account for ~30% of the optical-line fluxes of the [O II] λλ3727, 3729 and the [N II] λλ6548, 6584 doublets. In contrast, the DIG contamination on the higher-ionization transitions in the IR would be negligible. Additionally, this difference would be enhanced for large galaxies with an old stellar population that could have enriched the DIG with secondary nitrogen. We test this hypothesis by comparing the N/O optical-to-IR ratio with the gas density derived from the [S II] λλ6716, 6731 doublet in Figure 18. The sulfur doublet probes the gas density in the same ISM domain where the [N II] λλ6548, 6584 lines are produced, and therefore, it should be sensitive to the presence of DIG due to the low densities associated with this component. However, no correlation is found in Figure 18, meaning that the discrepancies in Δ(N/O) are not associated with a low-density gas component. Additionally, excluding the sulfur lines in the abundance computation with HCM does not result in significant differences in the N/O ratios obtained, as would be expected for DIG contamination affecting the sulfur line fluxes (e.g., Pilyugin et al. 2018). Thus, we conclude that DIG contamination does not significantly affect the optical-line fluxes.

The third scenario is the possible effect of dust obscuration on the optical-based determinations. Although optical-line fluxes were corrected by extinction estimated from the observed Balmer decrement values, uncorrected obscuration affecting the [O II] λλ3727, 3729 doublet would particularly affect the optical N/O abundances because the nitrogen lines are less affected by dust attenuation. This possibility is investigated in Figure 19, where Δ(N/O) is compared with the optical extinction A_V values derived from the Balmer decrement. No significant trend is observed, suggesting that uncorrected residual extinction cannot explain the differences seen in the N/O abundances.

An alternative explanation, more speculative, would imply that optical transitions are completely missing the embedded star-forming regions for the galaxies in our sample. Consequently, the optical lines would preferentially trace the gas in more external regions, which would be more exposed to enrichment with secondary nitrogen and biased against dust-embedded massive stars. In contrast, the gas traced by the IR transitions would be associated with lower N/O ratios due to the contribution from massive stars. In this scenario, the

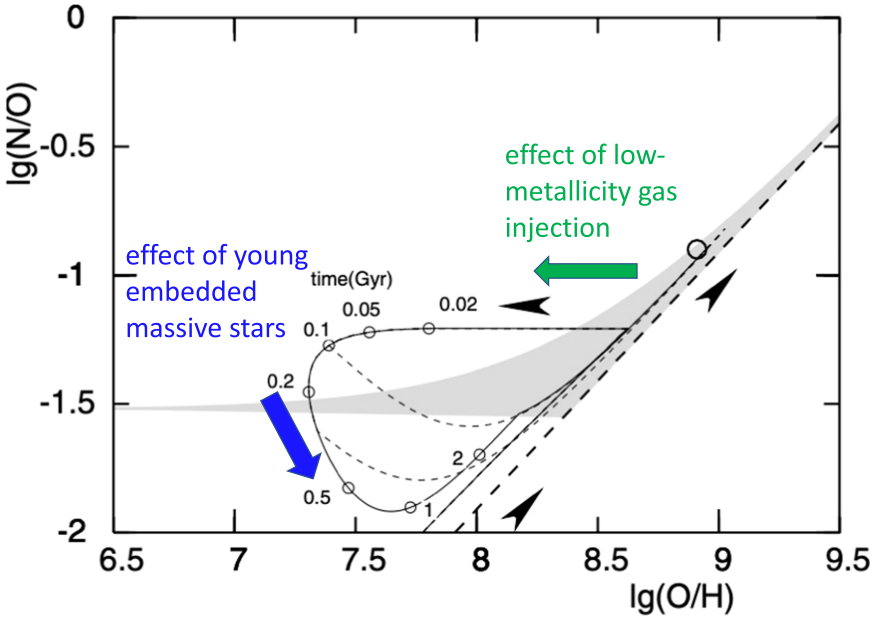

Figure 22. The time evolution of the extreme model from Köppen & Hensler (2005) with an infall rate of 100 galaxy masses per Gyr, starting at an age of 5 Gyr. The upper arrow indicates the effect of low-metallicity gas injection, while the lower arrow the effect of young embedded massive stars. The decrease in the N/O ratio (downward arrow) is due to the primary production of young massive stars, which preferentially produce oxygen compared to nitrogen. Adapted from Figure 3 of Köppen & Hensler (2005).

differences between optical and IR N/O abundances in galaxies would be a consequence of the chemical evolution process that may follow episodes of low-metallicity gas accretion from the circumgalactic medium or the external disk of the galaxy. This process has been modeled by Köppen & Hensler (2005), showing that the rapid decrease in oxygen abundance after the gas infall is followed by a sharp decrease in the N/O ratio due to the yields of the newly formed massive stars. The O/H and N/O increase at a later time due to the ongoing star formation and the secondary production of nitrogen from intermediate-mass stars, closing the loop in the N/O–O/H diagram (see Figure 22). As a matter of fact, evidence of gas accretion affecting the N/O ratios in the disks of nearby star-forming galaxies has been recently discovered (Luo et al. 2021). Local variations in the star formation efficiency could also play a role in explaining the different N/O ratios observed (Mollá et al. 2006; Florido et al. 2015; Kumari et al. 2018). If confirmed, this result would imply that the N/O ratios measured with IR lines are more genuine than those in the optical because they reflect the chemical abundances in the ISM gas phase including also the obscured regions not detected by optical tracers.

Although the cause of the optical-to-IR discrepancy is still unknown, we favor the abundances derived from the IR lines because these are virtually independent of dust and temperature effects. The optical-line emissivities present a strong dependency on the gas temperature (e.g., Figure 1 in Fernández-Ontiveros et al. 2021) and could be affected by, e.g., inhomogeneities in the gas nebula (Peimbert 1967), while the IR lines can provide more robust abundance estimates (e.g., Vermeij & van der Hulst 2002; Dors et al. 2013). On the other hand, our IR N/O determinations based on photoionization models are in agreement with the values obtained using the density-corrected N3O3n_e parameter introduced by Peng et al. (2021), as shown in Figures 20 and 21. The optical-to-IR abundance discrepancy analyzed in this work warns against the use of optical tracers to study the N/O abundances in galaxies at high redshift, e.g., using future James Webb Space Telescope observations of their rest-frame optical spectrum. These should be compared with measurements derived from the far-IR transitions redshifted in the submillimeter range and observed with ALMA or future facilities in this spectral range, when available.

7. Summary

We summarize here the main results of this paper.

1. We have reduced and analyzed new and archival spectra of the [O III] 52 μm and [N III] 57 μm lines in 29 galaxies collected by the SOFIA FIFI-LS spectrometer.
2. Using literature data from Herschel-PACS and ISO-LWS, we have assembled a sample of 47 galaxies, including 21 H II region/(U)LIRG galaxies and 19 Seyfert galaxies, including 1 LINER and 7 dwarf galaxies, for which we have full coverage of the [N III] 57 μm line and at least one of the two [O III] lines (at 52 μm or 88 μm).
3. We have complemented the [N III] and [O III] far-IR line observations of this sample with the mid- and far-IR lines useful for the characterization of the sample and the analysis carried out in this work aimed at the determination of the metallicity using IR spectra. In particular, we used the Spitzer-IRS and the Herschel-PACS spectra where available for the galaxies of the sample.
4. We have exploited various line ratios, namely the (2.2 × [O III] 88 μm + [O III] 52 μm)/[N III] 57 μm ratio, the [O III] 88 μm/[N III] 57 μm ratio, the [O III] 88 μm/[N II] 122 μm ratio, and the ([Ne II] 12.8 μm +[Ne III] 15.5 μm) to ([S III] 18.7 μm + [S IV] 10.5 μm) composite ratio, to map with the use of photoionization models their dependence on the metallicity, expressed as [12 + log(O/H)]. In other words, we assessed the use of these line ratios to measure the metallicity in galaxies.

5. We find that the determination of the (O/H) ratio with optical emission lines is consistent, within the errors, with its determination through IR fine-structure lines.
6. We find, in contrast, that the (N/O) determined abundance through optical lines is significantly different from that determined from the IR lines, especially for high values of (N/O) (N/O $\gtrsim -0.8$).
7. We explored whether a difference in the ionization structure mapped by the IR lines, which trace higher-ionization gas (O^{2+} and N^{2+}) with respect to the one mapped in the optical (O^{+} and N^{+}), could result in lower N/O ratios for the IR lines. However, we do not find a significant correlation between the $\Delta(N/O) = (N/O)_{OPT} - (N/O)_{IR}$ and the ionization indices.
8. We explored the possibility that the presence of diffuse ionized gas (DIG) in the ISM of galaxies could be responsible for this difference by searching correlations between the Δ(N/O) and the electron density as measured from different tracers (the [S II] $\lambda\lambda$6716,6731 lines, the [S III] 18 μm and 33 μm lines, and the [O III] 52 μm and 88 μm lines), but we do not find any statistically significant correlation.
9. We also searched the correlation between Δ(N/O) and the optical extinction $A_V$for a systematic underestimation of the correction for the optical extinction of the optical lines used to determine the (N/O) ratio, but we did not find any correlation.
10. We speculatively suggest that accretion of metal-poor gas from the circumgalactic medium could provide an explanation for the observed Δ(N/O) because the rapid decrease of the oxygen abundance during infall is followed by a decrease of the N/O ratio due to the primary production of young—possibly embedded—massive stars, which are preferentially traced by the IR diagnostics, while optical diagnostics would better trace the secondary production, when both N/O and O/H abundance ratios will increase.

This work is based on observations made with the NASA/DLR Stratospheric Observatory for Infrared Astronomy (SOFIA). SOFIA is jointly operated by the Universities Space Research Association, Inc. (USRA), under NASA contract NNA17BF53C, and the Deutsches SOFIA Institut (DSI) under DLR contract 50 OK 0901 to the University of Stuttgart. We thank the anonymous referee, who helped to improve this paper. J.A.F.O. and L.S. acknowledge financial support by the Agenzia Spaziale Italiana (ASI) under research contract 2018-31-HH0. J.A.F.O. acknowledges financial support from the Spanish Ministry of Science and Innovation and the European Union—NextGenerationEU through the Recovery and Resilience Facility project ICTS-MRR-2021-03-CEFCA. M.P.S. acknowledges support from the Comunidad de Madrid through the Atracción de Talento Investigador grant 2018-T1/TIC-11035 and PID2019-105423GA-I00 (MCIU/AEI/FEDER, UE). We acknowledge financial support from the NASA/SOFIA grant USRA 07-0239.

Facilities: SOFIA (FIFI-LS), Spitzer (IRS), Herschel (PACS)

Appendix A
Appendix Information

We present below our reductions for various galaxies included in Table 1. The complete figure set is available. Here we show an example for the galaxy NGC 1365 in Figure 23(a).

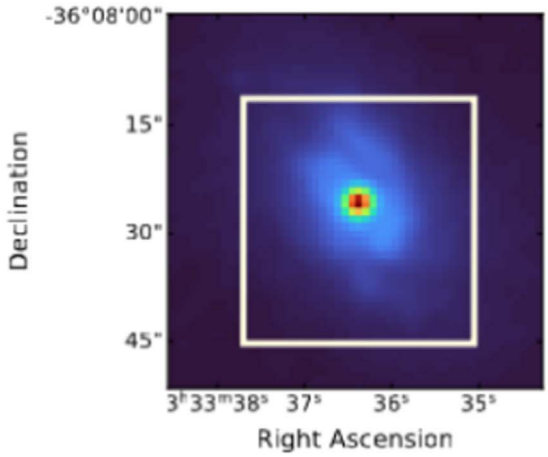

(a)

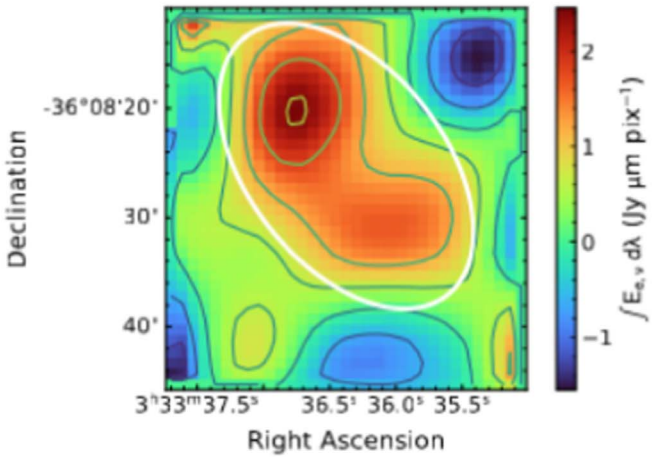

(b)

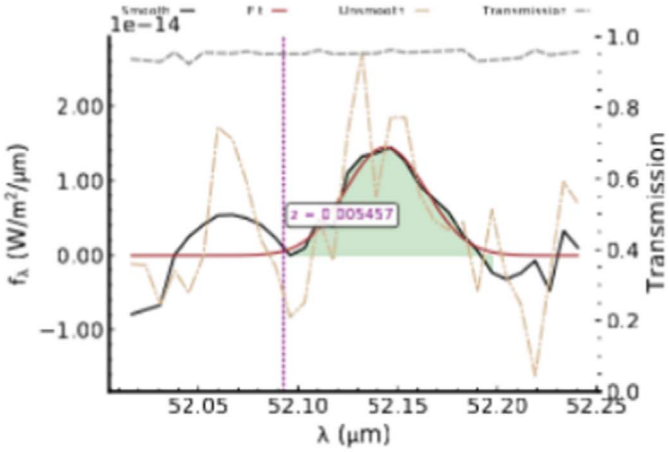

(c)

Figure 23. The 2MASS image (a) as well as 2D line map and 1D spectrum for [O III] 52 μm ((b) and (c), respectively) in NGC 1365. In this case, the optical center, located in the active galactic nucleus, lies in between the two peaks of the far-IR emission, which are on either side of the galactic disk.

(The complete figure set (22 images) is available.)

Appendix B
N/O Abundances for AGNs from IR Photoionization Models

Figure 24 shows the tight dependence of the N3O3 parameter, based on the ratio of [N III]57μm and [O III]52, 88μm lines, on the global N/O abundance ratio for the grid of AGN photoionization models using a power-law continuum index of $\alpha_{OX} = -0.8$ ($F_\nu \propto \nu^{\alpha_{OX}}$). Due to the similar ionization structure of nitrogen and oxygen elements, variations in log U have a small effect in the N3O3 parameter, allowing us to use a linear regression fit (black solid line; see Equation (5)) to determine the relative N/O abundances.

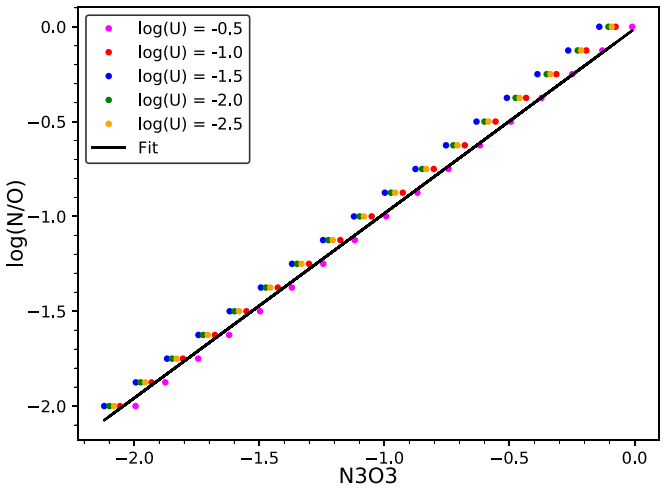

Figure 24. Predicted dependency of the inferred N/O abundances on the N3O3 parameter for AGN models with $n_e = 500$ cm^{-3} and log U in the −2.5 to −0.5 range. The solid black line shows a linear regression derived for the whole grid of models (see Section 4).

Appendix C
Δ(N/O) versus Density: IR Lines Diagnostics

In Figure 18 we explored the dependence of the Δ(N/O) on the electron density of the gas as measured from the optical [S II] λλ6716, 6731 doublet. We also explored if Δ(N/O) has some dependence on the electron density as derived from the IR fine-structure lines of [S III] and [O III]. We present the results here.

A similar trend to what is seen in Figure 18 is also present in Figure 25(a), where the Δ(N/O) value is plotted as a function of the electron density derived from the IR fine-structure lines of [S III] 18.7 μm and 33.5 μm. Also in this plot we see a higher Δ(N/O) value for higher gas densities; however, no correlation is present either for H II region/ULIRG galaxies and dwarf galaxies or for the total sample that includes Seyfert galaxies.

Figure 25(b) shows the Δ(N/O) value plotted as a function of the electron density as derived from the IR fine-structure lines of [O III] 52 μm and 88 μm. In this figure, if one considers only the H II region/ULIRG and dwarf galaxies and excludes the Seyfert galaxies, a decreasing trend of Δ(N/O) is found as a function of density. However, because of the large spread of the data and the poor statistics, no statistically significant correlation is found. We notice, however, that a decreasing trend of the Δ(N/O) value with the electron density, related to a higher value of $(N/O)_{OPT}$ at low densities, would indeed be expected from the presence of DIG. This is hot and low-density gas in the disk of galaxies and can be excited by relatively old stars, which have enough time to increase the N abundance through secondary production and thus would be also associated with higher $(N/O)_{OPT}$ values, while the IR lines would be less contaminated due to the higher excitation. This scenario would be in agreement with the conclusion by Peng et al. (2021).

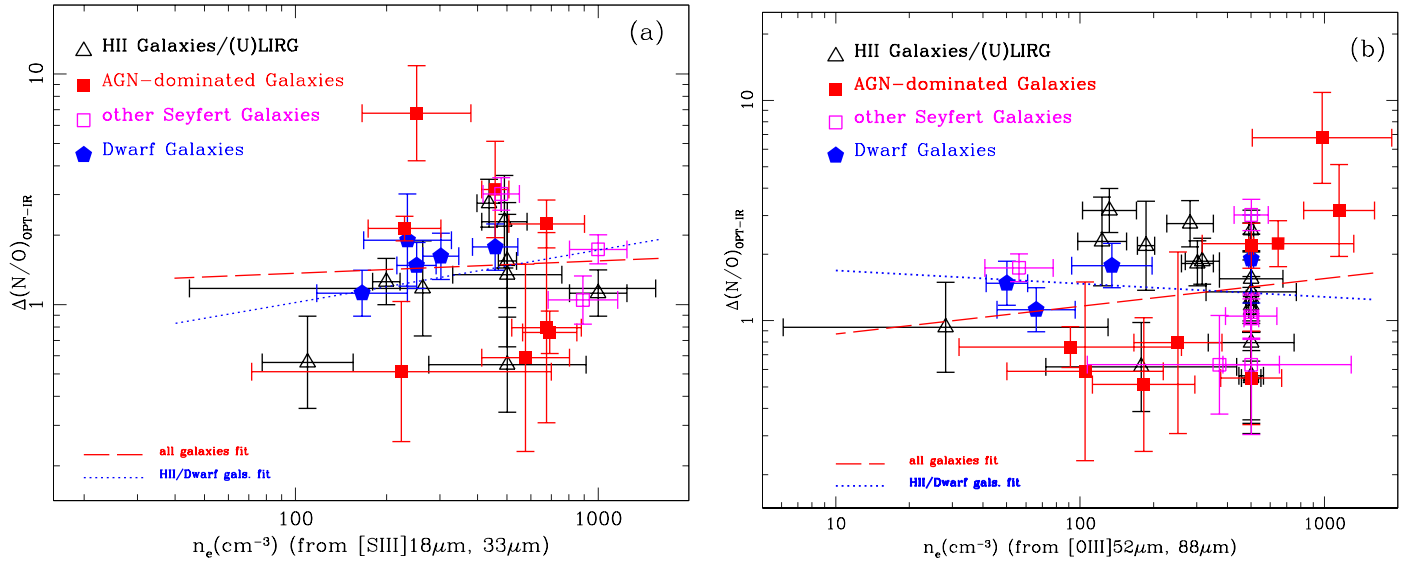

Figure 25. ((a): left) Logarithmic difference between the N/O ratio computed from IR emission lines and the N/O from optical lines vs. the electron density of the gas, as measured from the IR [S III]18.7 μm and 33.5 μm lines. The dotted line gives the fit for H II/ULIRG and dwarf galaxies: $y = (0.23 \pm 0.22) \cdot x - (0.45 \pm 0.56)$ ($\chi^2 = 0.47$, $R = 0.29$). A fit to all the data gives (shown as a dashed line) $y = (0.05 \pm 0.23) \cdot x + (0.03 \pm 0.60)$($\chi^2 = 1.97$, $R = 0.05$). ((b): right) Logarithmic difference between the N/O ratio computed from IR emission lines and the N/O from optical lines vs. the electron density of the gas, as measured from the IR [O III] 52 μm and 88 μm lines. The dotted line gives the fit for H II/ULIRG and dwarf galaxies: $y = -(0.06 \pm 0.13) \cdot x + (0.29 \pm 0.32)$($\chi^2 = 0.98$, $R = -0.10$). A fit to all the data gives (shown as a dashed line) $y = (0.12 \pm 0.12) \cdot x - (0.19 \pm 0.30)$($\chi^2 = 2.58$, $R = 0.17$).

ORCID iDs

Luigi Spinoglio https://orcid.org/0000-0001-8840-1551
Juan Antonio Fernández-Ontiveros https://orcid.org/0000-0001-9490-899X
Matthew A. Malkan https://orcid.org/0000-0001-6919-1237
Suyash Kumar https://orcid.org/0000-0003-4427-4831
Miguel Pereira-Santaella https://orcid.org/0000-0002-4005-9619
Borja Pérez-Díaz https://orcid.org/0000-0002-0939-9156
Enrique Pérez-Montero https://orcid.org/0000-0003-3985-4882
Alfred Krabbe https://orcid.org/0000-0002-8522-7006
William Vacca https://orcid.org/0000-0002-9123-0068
Christian Fischer https://orcid.org/0000-0002-7299-8661

References

Alonso-Herrero, A., García-Marín, M., Rodríguez Zaurín, J., et al. 2010, A&A, 522, A7
Amorín, R. O., Pérez-Montero, E., & Vílchez, J. M. 2010, ApJL, 715, L128
Armus, L., Charmandaris, V., Bernard-Salas, J., et al. 2007, ApJ, 656, 148
Baldwin, J. A., Phillips, M. M., & Terlevich, R. 1981, PASP, 93, 5
Bernard-Salas, J., Pottasch, S. R., Beintema, D. A., & Wesselius, P. R. 2001, A&A, 367, 949
Brauher, J. R., Dale, D. A., & Helou, G. 2008, ApJS, 178, 280
Calzetti, D., Harris, J., Gallagher, J. S. I., et al. 2004, AJ, 127, 1405
Clegg, P. E., Ade, P. A. R., Armand, C., et al. 1996, A&A, 315, L38
Colditz, S., Looney, L. W., Bigiel, F., et al. 2020, Proc. SPIE, 11453, 1145334
Cormier, D., Abel, N. P., Hony, S., et al. 2019, A&A, 626, A23
Cormier, D., Madden, S. C., Lebouteiller, V., et al. 2015, A&A, 578, A53
Dale, D. A., Smith, J. D. T., Armus, L., et al. 2006, ApJ, 646, 161
De Breuck, C., Weiß, A., Béthermin, M., et al. 2019, A&A, 631, A167
de Graauw, T., Haser, L. N., Beintema, D. A., et al. 1996, A&A, 315, L49
Díaz-Santos, T., Armus, L., Charmandaris, V., et al. 2017, ApJ, 846, 32
Dopita, M. A., & Evans, I. N. 1986, ApJ, 307, 431
Dors, O. L., Cardaci, M. V., Hägele, G. F., et al. 2015, MNRAS, 453, 4102
Dors, O. L., Hägele, G. F., Cardaci, M. V., et al. 2013, MNRAS, 432, 2512
Ferland, G. J., Chatzikos, M., Guzmán, F., et al. 2017, RMxAA, 53, 385
Fernández-Ontiveros, J. A., Armus, L., Baes, M., et al. 2017, PASA, 34, e053
Fernández-Ontiveros, J. A., Pérez-Montero, E., Vílchez, J. M., Amorín, R., & Spinoglio, L. 2021, A&A, 652, A23
Fernández-Ontiveros, J. A., Spinoglio, L., Pereira-Santaella, M., et al. 2016, ApJS, 226, 19
Fischer, C., Beckmann, S., Bryant, A., et al. 2018, JAI, 7, 1840003
Florido, E., Zurita, A., Pérez, I., et al. 2015, A&A, 584, A88
Gardner, J. P., Mather, J. C., Clampin, M., et al. 2006, SSRv, 123, 485
Griffin, M. J., Abergel, A., Abreu, A., et al. 2010, A&A, 518, L3
Henry, A., Scarlata, C., Domínguez, A., et al. 2013, ApJL, 776, L27
Herrera-Camus, R., Sturm, E., Graciá-Carpio, J., et al. 2018, ApJ, 861, 94
Hogarth, L., Amorín, R., Vílchez, J. M., et al. 2020, MNRAS, 494, 3541
Houck, J. R., Roellig, T. L., van Cleve, J., et al. 2004, ApJS, 154, 18
Imanishi, M., Maiolino, R., & Nakagawa, T. 2010, ApJ, 709, 801
Inami, H., Armus, L., Charmandaris, V., et al. 2013, ApJ, 777, 156
Izotov, Y. I., & Thuan, T. X. 1998, ApJ, 500, 188
Izotov, Y. I., Thuan, T. X., & Lipovetsky, V. A. 1994, ApJ, 435, 647
Kessler, M. F., Steinz, J. A., Anderegg, M. E., et al. 1996, A&A, 500, 493
Kewley, L. J., & Ellison, S. L. 2008, ApJ, 681, 1183
Kobulnicky, H. A., & Skillman, E. D. 1996, ApJ, 471, 211
Köppen, J., & Hensler, G. 2005, A&A, 434, 531
Kroupa, P. 2001, MNRAS, 322, 231
Kumari, N., James, B. L., Irwin, M. J., Amorín, R., & Pérez-Montero, E. 2018, MNRAS, 476, 3793
Leitherer, C., Schaerer, D., Goldader, J. D., et al. 1999, ApJS, 123, 3
Lequeux, J., Peimbert, M., Rayo, J. F., Serrano, A., & Torres-Peimbert, S. 1979, A&A, 80, 155L
Liu, X. W., Barlow, M. J., Cohen, M., et al. 2001, MNRAS, 323, 343
Luo, Y., Heckman, T., Hwang, H.-C., et al. 2021, ApJ, 908, 183
Ly, C., Malkan, M. A., Rigby, J. R., & Nagao, T. 2016, ApJ, 828, 67
Madden, S. C., Rémy-Ruyer, A., Galametz, M., et al. 2013, PASP, 125, 600
Maiolino, R., & Mannucci, F. 2019, A&ARv, 27, 3
Meléndez, M., Kraemer, S. B., Weaver, K. A., & Mushotzky, R. F. 2011, ApJ, 738, 6
Meynet, G., Maeder, A., Schaller, G., Schaerer, D., & Charbonnel, C. 1994, A&As, 103, 97
Mollá, M., García-Vargas, M. L., & Bressan, A. 2009, MNRAS, 398, 451
Mollá, M., Vílchez, J. M., Gavilán, M., & Díaz, A. I. 2006, MNRAS, 372, 1069
Moore, D., & Cohen, R. D. 1994, ApJ, 433, 602
Nagao, T., Maiolino, R., & Marconi, A. 2006, A&A, 459, 85
Nagao, T., Maiolino, R., Marconi, A., & Matsuhara, H. 2011, A&A, 526, A149
Pearson, C., Rigopoulou, D., Hurley, P., et al. 2016, ApJS, 227, 9
Peimbert, M. 1967, ApJ, 150, 825

Peng, B., Lamarche, C., Stacey, G. J., et al. 2021, ApJ, 908, 166
Pereira-Santaella, M., Rigopoulou, D., Farrah, D., Lebouteiller, V., & Li, J. 2017, MNRAS, 470, 1218
Perez, J., Michel-Dansac, L., & Tissera, P. B. 2011, MNRAS, 417, 580
Pérez-Montero, E. 2014, MNRAS, 441, 2663
Pérez-Montero, E., & Contini, T. 2009, MNRAS, 398, 949
Pérez-Montero, E., Contini, T., Lamareille, F., et al. 2013, A&A, 549, A25
Pérez-Montero, E., Dors, O. L., Vílchez, J. M., et al. 2019, MNRAS, 489, 2652
Pérez-Montero, E., & Vílchez, J. M. 2009, MNRAS, 400, 1721
Pilbratt, G. L., Riedinger, J. R., Passvogel, T., et al. 2010, A&A, 518, L1
Pilyugin, L. S., Grebel, E. K., & Kniazev, A. Y. 2014, AJ, 147, 131
Pilyugin, L. S., Grebel, E. K., Zinchenko, I. A., et al. 2018, A&A, 613, A1
Pilyugin, L. S., & Thuan, T. X. 2007, ApJ, 669, 299
Pilyugin, L. S., Thuan, T. X., & Vílchez, J. M. 2003, A&A, 397, 487
Poglitsch, A., Waelkens, C., Geis, N., et al. 2010, A&A, 518, L2
Pottasch, S. R., & Beintema, D. A. 1999, A&A, 347, 975
Spinoglio, L., & Malkan, M. A. 1992, ApJ, 399, 504
Temi, P., Marcum, P. M., Young, E., et al. 2014, ApJS, 212, 24
Torrey, P., Cox, T. J., Kewley, L., & Hernquist, L. 2012, ApJ, 746, 108
Tremonti, C. A., Heckman, T. M., Kauffmann, G., et al. 2004, ApJ, 613, 898
Tsujimoto, T., & Bekki, K. 2011, A&A, 530, A78
Vacca, W., Clarke, M., Perera, D., Fadda, D., & Holt, J. 2020, in ASP Conf. Ser. 527, Astronomical Society of the Pacific Conf. Ser., ed. R. Pizzo et al. (San Francisco, CA: ASP), 547
Vale Asari, N., Couto, G. S., Cid Fernandes, R., et al. 2019, MNRAS, 489, 4721
Veilleux, S., Rupke, D. S. N., Kim, D. C., et al. 2009, ApJS, 182, 628
Vermeij, R., & van der Hulst, J. M. 2002, A&A, 391, 1081
Vila-Costas, M. B., & Edmunds, M. G. 1993, MNRAS, 265, 199
Vilchez, J. M., & Pagel, B. E. J. 1988, MNRAS, 231, 257
Vincenzo, F., Belfiore, F., Maiolino, R., Matteucci, F., & Ventura, P. 2016, MNRAS, 458, 3466
Werner, M. W., Roellig, T. L., Low, F. J., et al. 2004, ApJS, 154, 1
Xia, J., Malkan, M. A., Ross, N. R., & Ancheta, A. J. 2018, ApJ, 869, 138